Energy 248 (2022) 123575

Contents lists available at ScienceDirect

Energy

journal homepage: www.elsevier.com/locate/energy

Mechanical property alterations across coal matrix due to water-CO_2 treatments: A micro-to-nano scale experimental study

Ang Liu, Shimin Liu*

Department of Energy and Mineral Engineering, G³ Center and Energy Institute, The Pennsylvania State University, University Park, PA, 16802, USA

ARTICLE INFO

Article history:
Received 24 December 2021
Received in revised form
20 February 2022
Accepted 21 February 2022
Available online 24 February 2022

Keywords:
Nanoindentation
Heterogeneity
FESEM-EDS
CO_2 adsorption
Supercritical CO_2

ABSTRACT

CO_2 sequestration in geological coal formations is a promising pathway to store a huge amount of CO_2 due to a strong CO_2 affinity on coal. It has been reported that CO_2 sorption can cause a strength reduction of coals. However, the mechanism-based understandings of CO_2-coal interactions induced alterations are still challenging in micro-to-nano scale. We conducted the combined grid-based nanoindentation tests and FESEM-EDS analyses to understand and quantify the mechanical property variations and distributions of coals in micro- or nano-scale due to its mineral and structural variations. We also quantified the mechanical property alterations induced by gaseous CO_2, $ScCO_2$, and $ScCO_2$-water mixture treatments at different treating durations. The combined results from the FESEM-EDS and XRD confirmed that the heterogeneity of two tested coal is prevailing at micro-to-nano scale and the corresponding mechanical properties are composition- and microstructure-dependent. The mechanical properties of coals can be altered by gaseous CO_2, $ScCO_2$, and $ScCO_2$-water mixture treatments primarily due to the organic carbon-CO_2 interactions and water hydration effects in wetted coals, or potentially due to the dissolution and precipitation of minerals occurred in fluid environment typically under the $ScCO_2$-water treatment condition.

1. Introduction

The excessive emissions of greenhouse gasses into the atmosphere have adversely been contributing to global warming and climate crisis [1]. Carbon dioxide (CO_2) sequestration, also known as carbon capture and storage (CCS), has been attracted much attention within the engineering community for the purpose of reducing carbon dioxide in the atmosphere [2]. CO_2 sequestration and/or storage in subsurface geological formations such as the depleted hydrocarbon reservoirs, aquifers, manmade underground cavity, coalbeds, and others is a proven way to store a huge amount of CO_2 [3–5]. CO_2 storage in mineable/deep un-mineable coal seam is one of the most economically viable for long-term CO_2 sequestration. Due to the relatively high affinity of CO_2 on coal, the competitive sorption process occurs after CO_2 is injected into coal seams. When CO_2 is injected into deep moist coal seams, it can easily become the super-critical CO_2 ($ScCO_2$) with the pressure and temperature higher than ~7.38 MPa and 31.04 °C at *in situ* conditions. Additionally, CO_2 sequestration can also be coupled with enhanced coalbed methane production and is expected to offer the economic incentive for CBM operators [6–8]. However, sorption-induced coal matrix swelling [9,10] and its associated effects in coal permeability and strength reduction have been identified as the main reasons controlling the low injectivity of CO_2 in coal seam. Coal matrix is known to be a polymer-like porous medium with developed pores instead of rigid grain-packed brittle material. Coal matrix can swell or shrink in response to CO_2 adsorption or desorption due to gas sorption-induced surface energy alternation and the induced structural changes can weaken coal strength and trigger localized discontinuities [9]. These consequences can be occurred due to the existence of moisture in coal [11,12]. The core-scale coal specimen is widely used to define the mechanical properties of coals as well as the associated alterations of mechanical property under different environmental conditions [13–15], which towards to upscale the quantified relations to field scale for engineering practices. However, gas/water sorption is a micro-to nano-scale behavior, a vague question is that to what scale the sorption-induced swelling effect can exert on the coal strength due to CO_2 uptake, and what are the combined effects on the coal strength caused by CO_2-water mixture uptake under the *in situ*

* Corresponding author.
E-mail address: szl3@psu.edu (S. Liu).

https://doi.org/10.1016/j.energy.2022.123575
0360-5442/

wetted condition. Fig. 1 shows the characteristics of coal structures from sub-nanoscale to core-scale. With the aid of optical and scanning electron microscopes, the polymer-like porous features of coal are obvious. Coal matrix contains rigid solid skeleton and developed pores in micro-to nano-scale instead of visible fractures or cleats in macro-to core-scale. By recalling the above question, how to understand the mechanical property alterations induced by the fluid-coal interactions occurring in sub- and nano-scale? Before we can mechanistically model and quantify the CO_2 or CO_2-water mixture induced transport and failure behavior in coals, we should define the mechanical properties variations due to CO_2 or CO_2-water mixture uptake, which is the focus of this study.

The effects of CO_2 adsorption on the mechanical properties of coals have been extensively investigated especially at the meso- or macro-scale. The influence of CO_2 adsorption on mechanical properties of coals were related to CO_2 pressure, phase state, coal ranks, CO_2 saturation time, type of test (*i.e.* uniaxial or triaxial stress condition) et al. Masoudian found that the elastic moduli and the strengths of coal specimens (cylindrical samples with 2.5 cm in diameter and 5 cm in length) can decrease up to 19% and 20% when the CO_2 is injected into the coal specimens under the triaxial stress condition [16]. Hol et al. found that an average reduction of uniaxial strength is around 59% for low rank coal while that for high rank coal is 71% with $ScCO_2$ treatment [17]. Perera et al. reported that the induced reductions in UCS and Young's modulus of bituminous coal caused by gaseous CO_2 adsorption can be up to 53% and 36%, while the $ScCO_2$ adsorption was observed to result in 40% greater UCS strength reduction and 100% greater Young's modulus reduction compared to gaseous CO_2 [7]. They explained that the strength reduction induced by gaseous CO_2 adsorption is because of coal matrix swelling, which causes physical expansion of the cleats and predisposing these structures to fail, resulting in the reduction of overall coal bulk strength. $ScCO_2$ adsorbs more readily than gaseous CO_2 and is thus associated with a more significant swelling effect, resulting in a higher reduction in coal strength. In addition, $ScCO_2$ has a greater potential as a solvent than gaseous CO_2 and therefore causes structural plasticization in coal, accounting for the additional Young's modulus decrease observed for $ScCO_2$. Sampath et al. reported that the coal strength decreased by 13.9% after 1d treatment of CO_2 saturation while further decrease in coal strength occurred very slowly with CO_2 saturation treatments for continuous 14 d and 45 d [18]. Based on these previous studies, it was evinced that CO_2 adsorption can cause the strength reduction of macro-scale coal specimens. However, the fractures and pores cannot be avoided in macro-to core-scale coal specimens and thus it is not clear how CO_2 adsorption can alter the rigid integrity of coal matrix? In addition, an intractable issue associated with the inch-sized coring specimens is the unstable physical and chemical heterogeneity even they were cored from the same bulk of coal. Also, the core specimen strength tests under uniaxial or tri-axial stress conditions are time-consuming, expensive, and most importantly they are not repeatable due to the heterogeneity of coal.

To understand the nano-to-micro-scale mechanical property evolution of coals caused by CO_2 treatments, nanoindentation test was proposed as the alternative method to measure the elastic modulus, hardness, and stiffness of coatings, thin films, and small volume bulk materials [19–22]. Nanoindentation test has also been performed to investigate the mechanical properties of various rocks such as shale, coal, sandstone, clay, granite, and quartz et al. [23–29]. For enhanced CO_2 sequestration, surfactants as additives that are added into nanofluids or hydraulic fracturing fluids for enhancing CO_2 transport and reducing formation damage are essentially very important [3] [–] [5]. Nanoindentation-enhanced screenings of hydraulic fracturing fluid additives was used [30], which provides us the insights to use this advanced technique to evaluate the mechanical property alterations across coal matrix due to water-CO_2 treatments in this work. From the $(P-h)$ curve acquired by nanoindentation test (P is the load, μ N and h is the deformation, nm), five important quantities can be measured, including the maximum load, nm), the displacement at the end of the loading stage (h_l, nm), the maximum displacement (h_m, nm), the final depth (h_f, nm), and the elastic unloading stiffness ($S = dP/dh$) defined as the slope of the upper portion of the unloading curve during the initial stages of unloading [31,32]. The

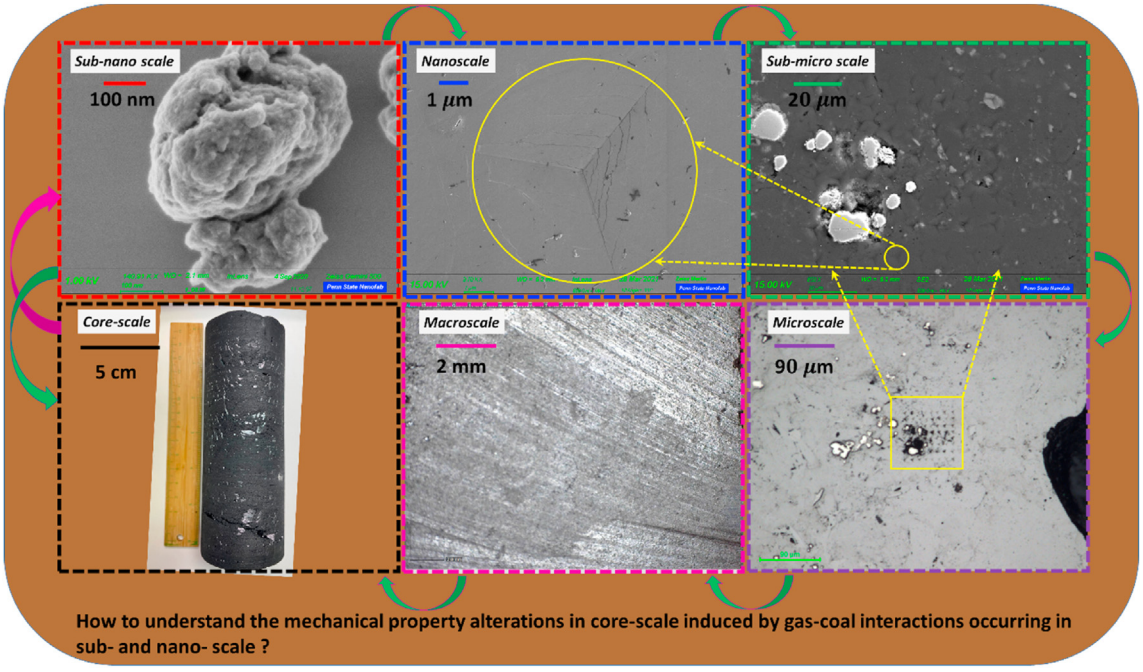

Fig. 1. Imaging of coal from sub-nanoscale to core-scale using optical and scanning electron microscopes.

deformation during the loading stage is supposed to be both elastic and plastic as the permanent hardness impression forms, while only the elastic deformations are recoverable during the unloading stage. The reduced modulus E_r, GPa, which combines the modulus of the indenter and the specimen, which can be expressed as [20]:

$$E_r = \frac{\sqrt{\pi}}{2\beta}\frac{S}{\sqrt{A_C}} \approx 0.17\frac{S}{h_c}, \quad (1)$$

where $A_c = 24.5h_c^2$ is the contact area, nm^2 and $\beta = 1.034$ is the geometric constant of a Berkovich indenter. The contact depth h_c can be calculated as $h_c = h_m - h_f$, nm. Further, the relations among the reduced modulus, and the Young's moduli and the Poisson's ratios of the specimen and of the indenter can be expressed as [33]:

$$\frac{1}{E_r} = \frac{1-\nu^2}{E} + \frac{1-\nu_i^2}{E_i}, \quad (2)$$

where E, E_i, υ, ν_i are the Young's moduli (GPa) and the Poisson's ratios (dimensionless) of the specimen and of the indenter, respectively.

In addition, the expression proposed by Oliver and Pharr was used to represent the hardness (H, GPa) from the load-displacement curve [20],

$$H = \frac{P_{max}}{A_C}, \quad (3)$$

Based on the above equations, a variety of Young's modulus and hardness of coal, ranges from 3.02 GPa to 9.04 GPa, with many others reported the nanoindentation moduli range between 4 and 7 GPa [27,34–36]. Shi et al. identified the mechanical strength difference on clay-rich and quartz-rich areas in shale sample and found that the mechanical strength substantially decreases in the clay-rich area because CO_2 adsorption and mineral dissolution happen after the $ScCO_2$ treatment, while the effects on quartz-rich area is minimal [37]. Zhang et al. measured the nanoindentation moduli of coal before and after water adsorption and found that the reductions in nanoindentation moduli can be up to 60–66% [38]. When gaseous CO_2 is injected into deep coal seams, it can easily become $ScCO_2$ and mix with formation water, and the $ScCO_2$-water mixture adsorption are expected to exert influences on the mechanical properties on coals but no published data are available so far. Also, the underlying mechanisms of the mechanical property alterations induced by CO_2 sorption or CO_2-water mixture uptake are still not fully understood due to the absence of mechanical properties at nano-or micro-scale.

We initially conducted the combined grid nanoindentation tests and Field Emission Scanning Electron Microscopy (FESEM)-EDS analyses to understand and quantify the mechanical properties of two fresh coals in micro-to nano-scale originating from the variability in their mineral and structural compositions. Two coals were then subjected to three different conditions for treatments including the gaseous CO_2, $ScCO_2$, and $ScCO_2$ plus water. Subsequently, the nanoindentation and FESEM-EDS measurements were conducted on those post-treated coal samples for comparisons. Through understanding the mechanical property alterations induced by the fluid-coal interactions occurring in sub- and nano-scale when coals are exposed to CO_2 or CO_2-water mixture, the results are expected to provide some insights on understanding the root cause of dynamic reservoir property changes (*i.e.* permeability and coal strength reductions) in the process of CO_2 sequestration from micro- or nano-scale. This study, therefore, supports the large-scale set-up of a CO_2 sequestration demonstration.

2. Materials and methods

2.1. Specimen preparation and XRD characterization

Two coal samples including one sub-bituminous coal (Herrin coal seam (I6)) from Illinois and one bituminous coal (Pittsburgh No.8 coal seam) from Pennsylvania were freshly collected at the mine sites. To characterize the mineralogical compositions of the two samples using X-ray diffraction analysis (XRD), the bulk samples were grounded below 325-mesh sieve using hand-grinding method. The Malvern Panalytical diffractometer (Malvern Panalytical Ltd.) was used to for XRD profile measurement. The two samples were used to detect scattering counts as a function of scattering angle two theta (2θ) at the room temperature. ZnO was added as an internal standard to quantify the amount of amorphous. Mineral compositions were obtained by profile fitting of the scattering curve, as detailed in Fig. A1 in Appendix A [39].

2.2. FESEM-EDS analysis and nanoindentation measurements

Coal is a sedimentary geomaterial with high organic content and thus it is a heterogeneous material comprised by a mixture of organic matter (macerals), inorganic matter (minerals), and pores/cleats network. The microscale indenter works under the micro- or nano-scale and thus the captured mechanical properties are expected to be highly correlated with the localized microstructures along with the solid skeleton. To approximately locate the landing positions of the indents and the constituting compositions or featured structures at those positions, the Zeiss Merlin FESEM and Oxford EDS detector (Ultim Max 100) are used to conduct the microstructure identification and elemental analysis. EDS can measure elemental variation, but cannot measure crystalline structure of different phases, *e.g.*, crystalline phase like minerals or amorphous phase like organic carbon. By combining with XRD results, the localized mineral/organic carbon compositions of indents can be identified, so does the crystalline structure of different phases, as illustrated in Appendix A. To acquire high resolution images and stable nanoindentation data, sample preparation process for FESEM-EDS analysis and nanoindentation test is extremely crucial. As shown in Fig. 2, a thin slice section with rough surface was initially cut from a piece of bulk coal (Fig. 2 (a)), then the thin slice section was put into a cylindrical mold with a diameter of ~38.11 mm for casting using epoxy resin that consists of the epoxy resin and hardener by weight of 5:1 (Fig. 2 (b)). The epoxy resin was allowed to fully cure with the setting time of around 72 h before moving from its curing position (Fig. 2 (c)), which will prevent the sample from spalling or damaging during the surface preparation step. The roughness of the sample surface was expected to be decreased by performing the grinding and polishing procedure using the MultiPrep™ Polishing System (Allied High- Tech Products, Inc.). The abrasive sandpapers with grit sizes of 320, 600, 800, and 1200 were sequentially used to polish the surface of the casted sample. The water-free and alcohol-based lubricants and ethanol were used at this stage to smooth this process and avoid potential mineral hydrations. Then, each sample was further polished to reach a finer surface using 1 μm, 0.25 μm polycrystalline diamond suspensions followed by 0.05 μm alumina suspension. To avoid potential mineral hydrations at this stage, the suspensions were ethylene- or glycol-based. Finally, the ethanol followed by the pressurized clean air were used to clean the sample surface for fine removal. The two prepared coal specimens were measured by nanoindentation followed by FESEM-EDS imaging and elemental analyses (Fig. 2 (d)). Subsequently, the cylindrical specimens were cut into four quadrants for fluid treatments, labeled as '1', '2',' '3', '4' as shown in Fig. 2 (e). The four quadrants were used for gaseous

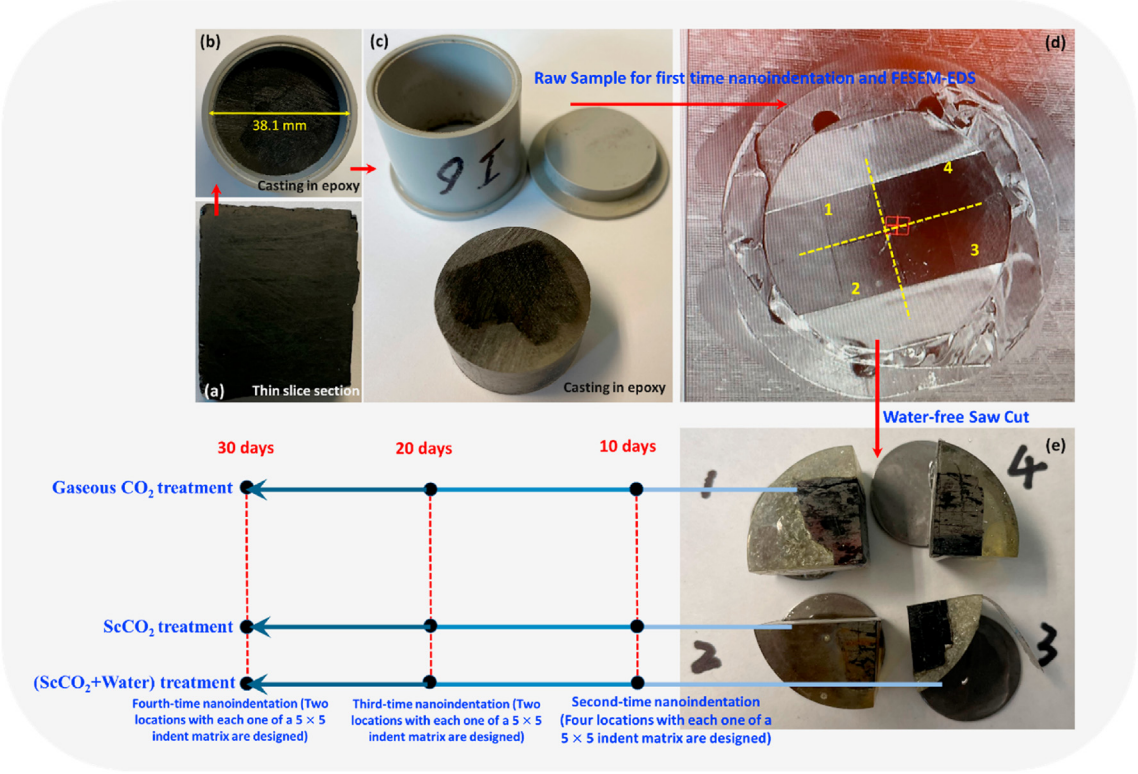

Fig. 2. Raw and treated sample preparations for nanoindentation test and FESEM-EDS.

CO_2, $ScCO_2$, $ScCO_2$-water mixture, and non-treatment, respectively. The fluid treatments were up to 30 days, but every 10 days the samples were taken out for nanoindentation tests. It should be noted that the samples were not dried before nanoindentation tests. At final stage, after completion of 30 days treatments, each specimen was again conducted both the nanoindentation and FESEM-EDS analyses.

Nanoindentation tests were conducted using Hysitron TI 980 TriboIndenter (Bruker Corp., US) at Penn State. The three-sided symmetric shape Berkovich indenter with the known Young's modulus (i.e. 1141 MPa) and the Poisson's ratio (i.e. 0.07) calibrated with thermal drift less than 0.05 nm/s. The load and displacement resolutions are 1 nN and 0.04 nm, respectively. The loading (0.5s) -holding (0.2s) -unloading (0.5s) scheme of each indent with the maximum load of 10000 μ N was applied.

2.3. CO_2 adsorption and water treatment process

In Section 2.2, we prepared the untreated coal specimens for the initial nanoindentation test and FESEM-EDS measurements. To understand the effects of gaseous CO_2, $ScCO_2$, and $ScCO_2$-water treatments on the mechanical property alterations on coals, the experimental scheme for the treatments was designed and shown in Fig. 3. Four quadrants were crosscut from each one of the two samples and were correspondingly loaded into different high pressure treating vessels with different treatment conditions. The entire experimental setup was immersed into water bath with the temperature of 36 $^{\circ}C$ $\pm 0.1^{\circ}C$, which is over the critical temperature at ~31.04 $^{\circ}C$. Pressure vessel 1 was flooded with gaseous CO_2 with pressure at around 500 psi. Pressure vessel 2 was pumped into supercritical CO_2 with pressure at around 1400 psi. Pressure vessel 3 was initially poured with High Performance Liquid Chromatography (HPLC) water and then injected supercritical CO_2 with pressure at around 1400 psi. The pressure transducers were installed and kept monitoring the pressures. As illustrated in Fig. 2, the treatment duration can be up to 30 days and every 10 days the specimens were taken out for nanoindentation tests. To minimize the air exposure time, the nanoindentation tests at 10 days and 20 days were completed within 6 h. After the nanoindentation tests, the samples were loaded back into the high-pressure vessels and further treated by injecting the CO_2 with the pressure backup to the designed pressure value.

3. Results

3.1. Mineralogical compositions in two coals

The XRD analyses of the two coals were summarized in Table 1. The bituminous coal P8 has the maximum carbon content of ~96%, compared with coal I6 of ~95.72%. Both two coals contain silicates minerals such as kaolinite (~1.69% in coal I6, ~1.45% in coal P8) and quartz (~1.69% in coal I6, ~1.67% in coal P8), and sulphides pyrite (~0.34% in coal I6, ~0.44% in coal P8). Other minerals including calcite (~0.11% in coal I6), muscovite (~0.22% in coal P8), and gypsum (~0.45% in coal I6) also present in two coals. Since the EDS measurements can be used to recognize the elemental compositions of the landing positions of the indents through FESEM, the localized minerals under the indents and their vicinities can be further identified by matching with the mineralogical compositions in three coals from Table 1. The analysis process of mineral identifications through XRD and EDS techniques is shown in Appendix A.

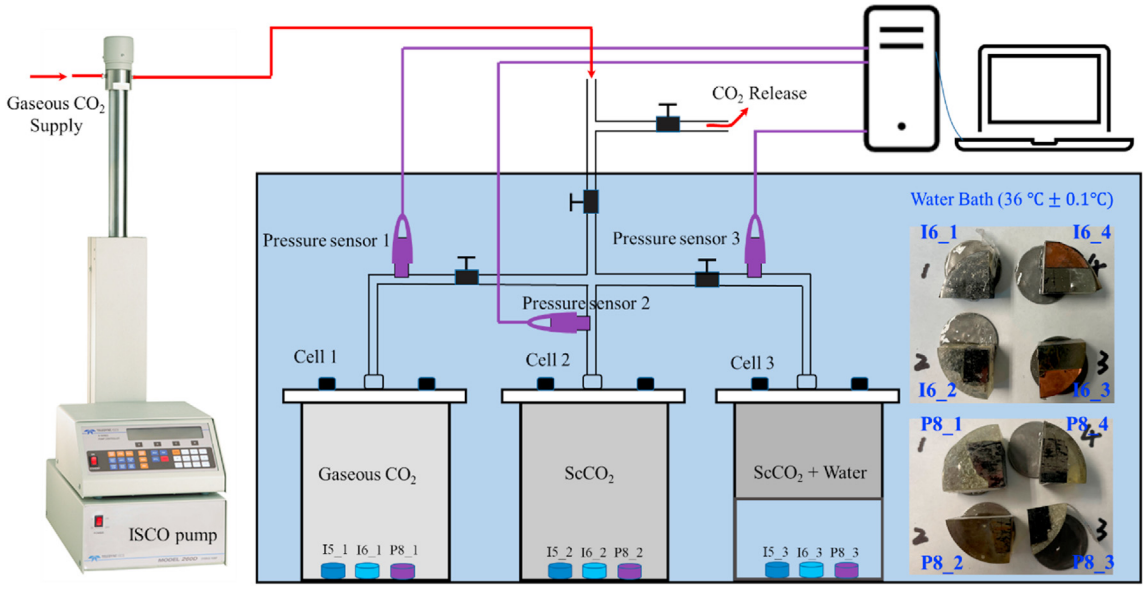

Fig. 3. CO_2 adsorption and water treatment process on coals.

Table 1
Weight percentage of the mineralogical compositions in coal samples (wt%).

Samples	Amorphous	Silicates		Sulphides	Carbonates	Phyllosilicate	Sulfate	
	Organic Carbon	Kaolinite	Quartz	Pyrite	Calcite	Muscovite	Szomolnokite	Gypsum
I6 (sub-bituminous)	95.72	1.69	1.69	0.34	0.11	–	–	0.45
P8 (bituminous)	96.00	1.45	1.67	0.44	0.22	0.22	–	–

3.2. Morphological characteristics and localized mineral compositions at the indents

The localized morphological characteristics, and organic/mineral compositions at the indents can be probed and identified, as shown in Fig. B1 in Appendix B. Before pressure and fluid treatments, a total of 256 indents was measured for each coal specimen (I6 and P8). For I6 coal specimen, it can be observed that some of the indents landed on regions distributed with kaolinite-rich minerals at all four locations and three indents ran into quartz-rich regions. By comparing with coal I6, the surface morphology of coal P8 is relatively homogeneous and most of indents landed at organic carbon regions except for the third location 'P8_P3(Initial)' distributing with certain kaolinite-rich minerals. After gaseous CO_2 adsorption and pressure treatments, eight locations (four locations after 10 days, two locations after both 20 days and 30days, as shown in Fig. 2) were selected to conduct nanoindentation tests for both coals I6 and P8. The same scheme was replicated for samples under both $ScCO_2$ and $ScCO_2$-water mixture treatments. As examples, after a 10-day treatment with gaseous CO_2 treatment, majority of indents on coal I6 landed on organic carbon rich regions without encountering with many minerals, while the indents landed on regions enriched with kaolinite minerals after both 20days and 30 days treatments. It is expected that the compositional difference at those landing sites of indents should reflect the variation of the mechanical properties of coals. Thus, the composition-based quantitative analyses could offer a unique site-specified comparison and quantification, which is the major technological innovation of this study. Unlike the traditional bulk mechanical tests (macro-scale to core-scale measurements reflecting statistical average of changes) using UCS, acoustic emission test, triaxial test et al., we can distinguish the composition-based property variation in micro- to nano-scale offering the micro-mechanism deterioration with fluid treatments. The microscopic insights may provide the mechanistic deterioration intensity and variation. These evidences could direct us to clarify the mechanical property alterations induced by the fluid-coal interactions occurring in sub- and nano-scale when coals are exposed to CO_2 or CO_2-water mixture, the results are expected to provide some insights on understanding the root cause of dynamic reservoir.

3.3. Hardnesses and Young's moduli alterations due to different fluid treatment conditions

Based on Eqs. (2) and (3), the hardnesses and Young's moduli of two coals were estimated from the load-displacement curves, as plotted in Figs. (4) and (5). In Fig. 4, hardness alterations on each one of two coals caused by different fluids (gaseous CO_2, $ScCO_2$, and $ScCO_2$-water mixture) as well as treatment time were compared. Without any fluid treatment, the hardness for coal I6 ranges from ~0.16 GPa to ~0.67 GPa, from ~0.48 GPa to ~0.71 GPa for coal P8. After 10-day, 20-day and 30-day gaseous CO_2 treatments, the hardness of coal I6 ranges from ~0.26 GPa to ~0.38 GPa, from ~0.25 GPa to ~0.45 GPa, and from ~0.29 GPa to ~0.71 GPa as shown in Fig. 4a. Compared with raw sample without treatment, an obvious decrease in hardness after the 10-day treatment and then increases in hardness after the 20-day and 30-day treatments were observed. We wanted to point out that the alterations effects induced by gaseous CO_2 treatment cannot simply compare because of the indent-site-specified mineralogical differences before and after treatments. By recalling the visualizations and composition identifications of indents in Fig.B1, most of indents on initial coal I6

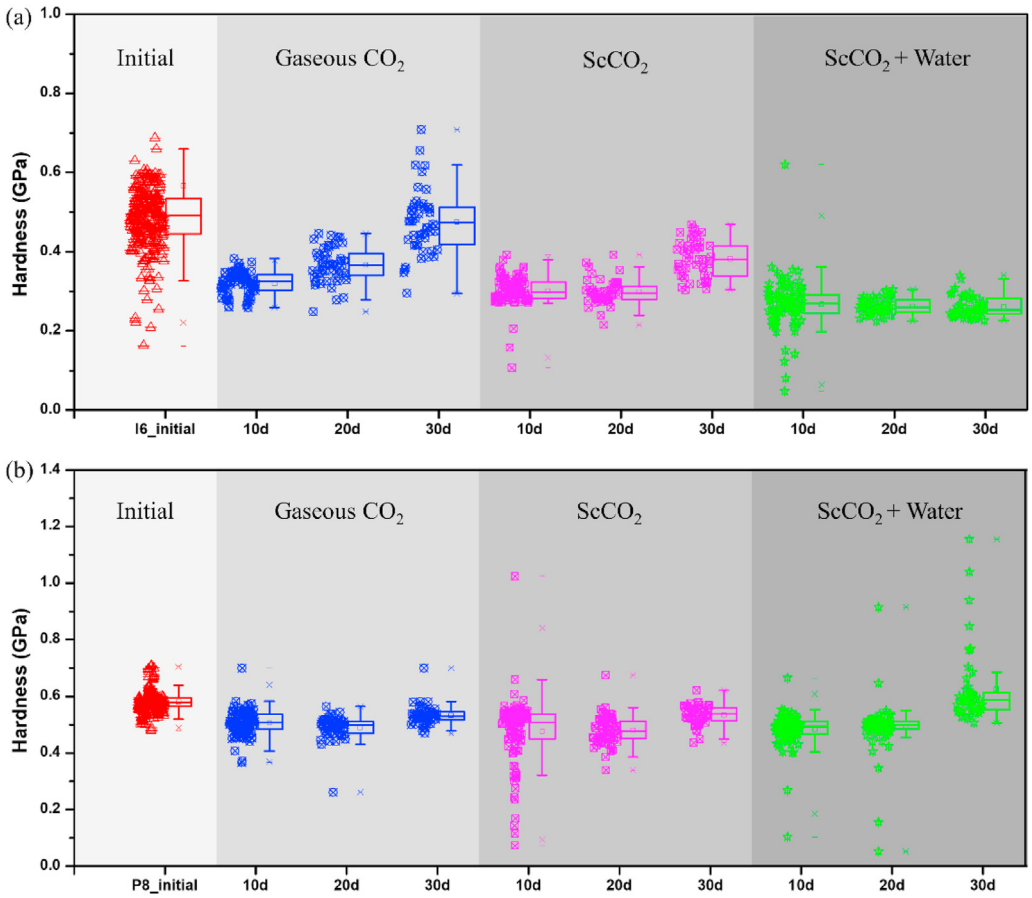

Fig. 4. Alterations on hardness of two coals under different treatment conditions. (a) coal I6; (b) coal P8.

landed on kaolinite-rich minerals, while the 10-day data mainly captured the mechanical properties of organic carbon rich indents and this may be the reason why there was an apparent drop in hardness and modulus as shown in Fig. 4a. As comparison, the 20-day and the 30-day indents landed on regions of kaolinite-rich mineral sites.

Statistically, the effects of gaseous CO_2 treatment on the mechanical alterations can be compared between the initial and the 30-day data due to both sites have similar mineralogical composition. The results indicate that the mechanical alteration is not apparent for kaolinite-rich areas as shown in Fig. 4a. For P8 coal, the hardnesses range from ~0.37 GPa to ~0.70 GPa, from ~0.26 GPa to ~0.56 GPa, and from ~0.47 GPa to ~0.70 GPa after 10-day, 20-day and 30-day treatments in Fig. 4b. Compared with coal I6, except for the third location 'P8_P3 (Initial)' containing more kaolinite-rich minerals, all the other three locations were landed on organic-carbon rich sites. The hardness of ~0.48 GPa—~0.71 GPa for coal P8 at initial testing site statistically indicates the mechanical properties of organic carbon rich composition, and it is noted that there are decreases in hardness after 10-day, 20-day and 30-day gaseous CO_2 treatments. It is apparent that a 10-day treatment time can provide enough interaction time for gaseous CO_2 because no further hardness reduction beyond 10-day treatment. Here, we want to pointed out that this coal hardness reduction is the surficial mechanical alteration after gas being removed. Thus, the mechanical property alterations reported here only indicate the irreversible properties changes. It is not ideal for mechanical alteration measurements under the fluid transport because it is not feasible to measure nanoindentation under high pressure.

For $ScCO_2$ adsorption treatment, the hardness of coal I6 ranges from ~0.11 GPa to ~0.39 GPa, from ~0.22 GPa to ~0.39 GPa, and from ~0.30 GPa to ~0.47 GPa with the 10-day, 20-day and 30-day treatments as shown in Fig. 4. The landing position of indents on coal I6 after treatments mainly distributed on regions with kaolinite-rich regions, which makes it comparable on the alteration effects induced by $ScCO_2$ adsorption treatments. The obvious decreases in hardness on kaolinite-rich regions over the 30-day treatments can be observed. By comparing with the alterations induced by gaseous CO_2 treatment, the $ScCO_2$ treatments could have an intensified the hardness reduction of coal I6. This may attribute to the stronger $ScCO_2$ uptake capacities of coal, as also evinced by the data from coal P8. The hardness of coal P8 ranges from ~0.07 GPa to ~1.02 GPa, from ~0.34 GPa to ~0.67 GPa, and from ~0.44 GPa to ~0.62 GPa after the 10-day, 20-day and 30-day treatments. As illustrated in Fig.B1, the landing locations of indents on coal P8 after 10-day, 20-day and 30-day treatments mainly landed on regions with encountering obvious clusters of minerals such as quartz or kaolinite et al. Unlike the $ScCO_2$ adsorption induced obvious changes on the mechanical properties of coal I6, slight decrease in hardness from all these three periodical measurements were observed for coal P8 by comparing with the sample without treatment. This is because the interactions between $ScCO_2$ and coal are mainly initiated by the organic-carbon compositions and $ScCO_2$ instead of the kaolinite-rich compositions.

For '$ScCO_2$+water' treatment condition, the hardness of coal I6 ranges from ~0.05 GPa to ~0.62 GPa, from ~0.22 GPa to ~0.30 GPa, and from ~0.23 GPa to ~0.34 GPa after the 10-day, 20-day and 30-day treatments. Comparing with gaseous CO_2 and $ScCO_2$

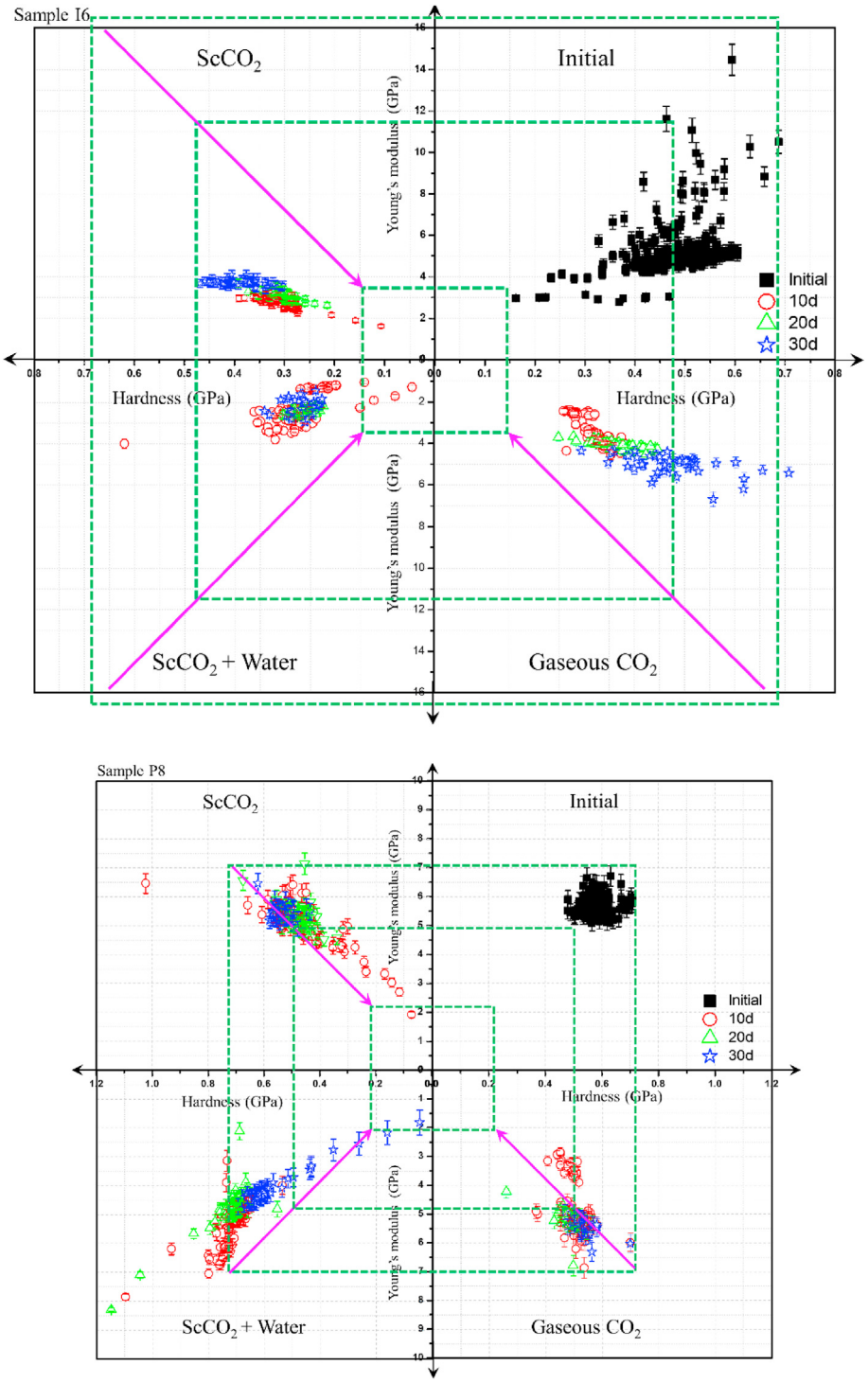

Fig. 5. Alterations on Young's modulus of two coals under different treatment conditions. First quadrant shows Young's moduli of raw coal. Second quadrant: after $ScCO_2$ treatment. Third quadrant: after 'ScCO2+water' treatment. Fourth quadrant: after gaseous CO_2 treatment. Three green squares are plotted for easy comparisons on the variations of Young's moduli.

treatment conditions, the '$ScCO_2$+water' treatment severely deteriorates the hardness of coal I6. This apparent hardness decrease could be due to the complex water-gas-coal interactions. To our best knowledge, water hydration in specimens under '$ScCO_2$+-water' treatment could be the primary reason. As shown in Fig. 2 (b), the specimens were casted using epoxy resin, which causes only one surface of the specimen is exposed to '$ScCO_2$+water' treatment and thus can enhance water suction into the specimen. It is highly possible that water hydration occurs inside the unsaturated specimens. Since we measured the nanoindentations on specimens after every 10-day treatment period and the nanoindentation tests were completed within 6 h, which implicitly indicates that most of the water still was still sucked and holding in the substrate. The wetted substrate is expected to become relatively

soft, and which can decrease the quantified hardness through nanoindentation test conducted on the coal surface in micro-to nano-scale.

Potentially, the CO_2 dissolves in water can change the acid-based equilibrium which can trigger the dissolution and precipitation of minerals, as shown in the below equations [40,41]. That is, the combined effects of organic carbon- CO_2 interactions and dissolution and precipitation of minerals induced by acid-based fluid environment would alter the mechanical properties of coal.

$$H_2O + CO_2 \leftrightarrow H_2CO_3 \leftrightarrow H^+ + HCO_3^- \quad (4)$$

$$HCO_3^- \leftrightarrow H^+ + CO_3^{2-} \quad (5)$$

$$CaCO_3\ (\text{Calcite}) + H^+ \leftrightarrow Ca^{2+} + CO_2 + H_2O \quad (6)$$

$$SiO_2\ (\text{Quartz}) + H^+ \leftrightarrow Si_{4+} + H_2O \quad (7)$$

The above statement can be further evinced based on the data of coal P8. The landing locations of indents on coal P8 after 10days', 20days' and 30days' treatments with '$ScCO_2$+water' mainly landed on the organic carbon rich regions. After treatment, the hardness of coal P8 ranges from ~0.10 GPa to ~0.66 GPa, from ~0.05 GPa to ~0.92 GPa, and from ~0.51 GPa to ~1.16 GPa after 10days, 20days and 30days, respectively. The changes on the hardness of coal P8 are not significant, which is mainly because the organic carbon- CO_2 interactions dominate the alterations while the dissolution and precipitation of minerals induced by acid-based fluid environment were not obvious because of the landing positions of indents do not rich in minerals.

In terms of the reduced moduli calculated from indentation tests, the Young's moduli for coal samples before and after treatments can be estimated based on Eq. (2) with known Poisson's ratios. However, we cannot measure the Poisson's ratio from the nanoindentation test, and thus the Poisson's ratios including 0.20, 0.25, 0.30, 0.35 and 0.40 were assumed for each indent case and then the error caused by the Poisson's ratio is expected to be calculated using the standard deviation (SD). The average of the Young's modulus calculated from the different Poisson's ratios and the associated standard deviation was plotted with respect to the hardness, as shown in Fig. 5. To compare Young's moduli of raw coal first quadrant of Fig. 5) and treated coals using different fluids (gaseous CO_2 – fourth quadrant, $ScCO_2$ -second quadrant, and '$ScCO_2$+water' – third quadrant in Fig. 5), the distributions of Young's moduli were merged together in Fig. 5. The alterations of mechanical properties induced by fluid treatments were analyzed and plotted by dash green squares and purple arrows in Fig. 5. The outermost and innermost squares were used to set the upper and lower limits for tested Young's moduli. For I6 coal specimen, the initial Young's modulus ranges from ~2.79 GPa to ~14.47 GPa with an average of ~5.34 GPa, while the Young's moduli range from ~2.39 GPa to ~6.67 GPa with an average of ~4.04 GPa after gaseous CO_2 treatment, from ~1.61 GPa to ~4.10 GPa with an average of ~3.04 GPa after $ScCO_2$ treatment, and from ~1.04 GPa to ~4.00 GPa with an average of ~2.37 GPa after '$ScCO_2$+water' treatment. It shows that all the treatments are expected to cause the reductions in the average magnitudes of Young's moduli, among which the most severely reduction of around 2.25 times was induced by '$ScCO_2$+water' treatment, followed by the $ScCO_2$ treatment of about 1.76 times and gaseous CO_2 treatment of around 1.32 times. As analyzed before, the organic carbon-$ScCO_2$ interactions is stronger than that of the organic carbon-gaseous CO_2 interactions, and further the '$ScCO_2$+water' treatment will initiate water hydration in specimens which can potentially decrease the strength of the substrate, and possibly initiate the acid-based fluid environment causing the dissolution and precipitation of minerals. For coal P8, the initial Young's modulus ranges from ~5.09 GPa to ~6.72 GPa with an average of ~5.73 GPa, while the Young's moduli range from ~2.85 GPa to ~6.86 GPa with an average of ~5.06 GPa after gaseous CO_2 treatment, from ~1.92 GPa to ~7.14 GPa with an average of ~5.25 GPa after $ScCO_2$ treatment, from ~1.45 GPa to ~3.92 GPa with an average of ~2.66 GPa after '$ScCO_2$+water' treatment. The data shows that very limited changes on the mechanical properties of coal P8 were caused by gaseous CO_2 treatment with a reduction of ~12% and $ScCO_2$ treatment with a reduction of ~8% respectively, while very significant reduction of around ~2.15 times caused by '$ScCO_2$+water' treatment. If we only consider the data from Table 1, coal P8 is more organic-carbon rich than coal I6 and it should show more obvious changes on Young's moduli after treatments especially induced by gaseous CO_2 and $ScCO_2$. However, if we recall the identification results of compositions at those landing positions of indents under different treatment conditions, our explanations of data for coal I6 are still valid. From Fig.B1, the initial 256 indents mainly landed on organic-carbon rich regions, while majority of indents landed on regions enriched with kaolinite mineral after gaseous CO_2 treatment for 10-day, 20-day and 30-day treatments. The existence of kaolinite mineral to some extend influence the matrix swelling/shrinkage effects induced by gaseous CO_2 sorption on coal. It is presumed that the $ScCO_2$ treatment should cause more severe reduction in Young's modulus on coal P8 than the gaseous CO_2 sorption because of the strong sorption capacity of coal to $ScCO_2$. However, if we visualize the landing positions of indents on coal P8 after $ScCO_2$ treatment for 10-day, 20-day, and 30-day, it can be found that the clusters of quartz-rich minerals encounter with the indents and thus the matrix swelling/shrinkage effects induced by $ScCO_2$ on coal at these regions were weak and the quantified reductions in Young's moduli at these regions were limited. By looking at the reductions in Young's moduli caused by $ScCO_2$+-water' treatment, the alteration were found to be significant, which was due to the combined effects of organic carbon-$ScCO_2$ interactions and water hydration effects in wetted coals, or potentially due to the dissolution and precipitation of minerals occurred in fluid environment typically under the $ScCO_2$-water treatment condition based on Eqs. (4), (5) and (7).

3.4. Deformations beneath the pointed indenter during loading-holding-unloading

For the nanoindentation test using the loading (0.5s) - holding (0.2s) -unloading (0.5s) scheme, the depth of the indenter at the end of the loading stage (h_l), the maximum displacement (h_m), and the final depth (h_f) can be captured. The depth h_l is the deformation of coal under pointed indenter at the end of the loading stage, which incorporates both the elastic and plastic responses under the loading. At the holding stage, the maximum displacements (h_m) reached under the constant maximum load and the creep deformation can be developed for deepening the deformation at this stage. For unloading stage, the deformation starts to recover till to the final displacement (h_f) upon the load vanishes. The maximum deformations on samples before and after different fluids (gaseous CO_2, $ScCO_2$, and $ScCO_2$-water mixture) treatments using the pointed loads peak at 10000 μ N in 0.5s were plotted in Fig. 6. After each periodical treatment, the average deformation (h_l) at the end of the loading stage were calculated from all the indents and the standard deviation (Std Dev) were calculated. For coal I6 and coal P8, the average deformation h_l at initial time are ~1160.20 nm and ~1089.11 nm, respectively. After gaseous CO_2 treatment, the average deformation h_l for coal I6 and coal P8 are ~1362.11 nm and ~1132.88 nm (10-day treatment), ~1263.21 nm and ~1106.56 nm

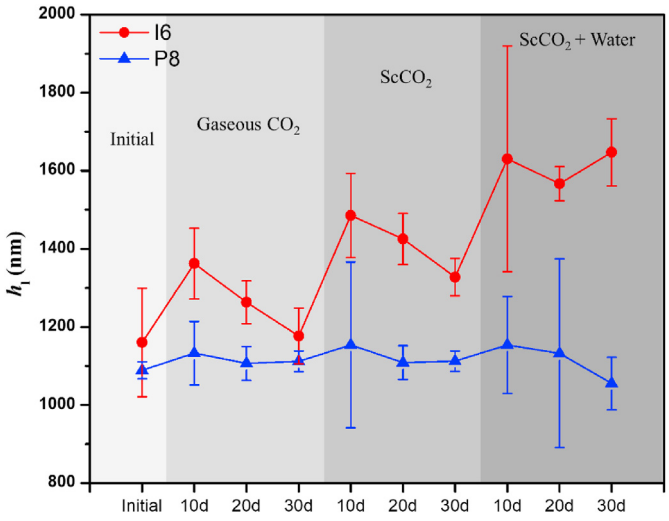

Fig. 6. Maximum deformation (h_l) at the end of the loading stage.

(20-day treatment), and ~1176.96 nm and ~1111.88 nm (30-day treatment). After $ScCO_2$ treatment, the average deformation h_l for coal I6 and coal P8 are ~1485.50 nm and ~1153.89 nm (10-day treatment), ~1425.11 nm and ~1108.49 nm (20-day treatment), and ~1327.41 nm and ~1112.46 nm (30-day treatment), and which are ~1630.44 nm and ~1153.95 nm (10-day treatment), ~1566.88 nm and ~1132.47 nm (20-day treatment), and ~1647.11 nm and ~1055.28 nm (30-day treatment) for coal I6 and coal P8 due to $ScCO_2$-water mixture treatment. It can be observed that an obvious increase in the deformation h_l under the pointed loads peak at 10000 μ N from initial status to gaseous CO_2 condition, $ScCO_2$ condition, and then the $ScCO_2$-water mixture condition for coal I6. For coal P8, the changes of the average deformation h_l under different treatment conditions are less obvious than that of coal I6 does, which is mainly because the occurrence of mineral compositions at the landing positions of periodical indentation tests, as explained in Fig.B1. The reason behind this trend can also be explained due to the alterations of mechanical properties such as the hardness and Young's modulus, as illustrated in Figs. (4) and (5). The harder the coal is, the smaller the deformation h_l is expected to be. The changes of deformations h_l can provide us the direct understandings on how the CO_2-coal interactions influence the localized deformations or failures.

The findings in Fig. 6 have direct application for providing mechanism-based quantifications of engineering encountered problems during CO_2 sequestration and enhanced coalbed methane recovery via CO_2 sequestration. As an example, hydraulic fracturing has been widely used to increase the hydraulic conductivity of the coal formation for CO_2 sequestration or enhanced coalbed methane recovery via CO_2 sequestration. The hydraulic fracturing process involves the injection of a high-pressure fluid(s) into the formation to initiate and create fractures to unlock the hydrocarbons by ensuring hydraulic conductivity through artificial fracture creation, as shown in Fig. 7 (a). As shown in Fig. 7 (b), the propping agents (sieved sand or ceramic proppants) are added to the injected fluid to keep both induced and natural fractures open after flowback. Hydraulic conductivity, representing by the fracture width, is directly influenced by the sandwiching stress on proppant packs because which can lead to proppant crushing and embedment. Under the *in situ* stress condition, the loading deformations h_l on proppant or coal caused by the pointed load on proppant initiated by stressed coal seam or potential pointed load on coal induced by stressed proppant. As consequences, the loading deformation under the dynamic stress condition may cause proppant damages include proppant crushing (proppants 'P2' and 'P3'), proppant embedment (proppant 'P1') when the loading deformations h_l exceed thresholds, as shown in Fig. 7 (c) and (d). Even at the stable gas injection/production periods, creep deformations can be further caused on the loading deformation till to the maximum h_m, as shown in Fig. 7 (e). As results, the proppant damages may create formation fines in micro-or nanoscale and results in excessive loss of fracture conductivities. From this point, it seems the possibility of proppant damages or coal failures in coal I6 is higher than that of coal P8 does under the same *in situ* stress and gas pressure condition.

The loading stage incorporates both the elastic and plastic responses under the loading. At the holding stage, the maximum displacements (h_m) reached under the constant maximum load and the creep deformation can be developed. The creep deformations induced by the constant load (10000 μ N) at the holding stage were represented as ($h_m - h_l$) and plotted in Fig. 8. For coal I6 and coal P8, the average deformations of $h_m - h_l$ at initial time are ~18.6 nm and ~31.38 nm, respectively. After gaseous CO_2 treatment, the average deformations of $h_m - h_l$ for coal I6 and coal P8 are ~19.31 nm and ~30.87 nm (10-day), ~25.66 nm and ~32.51 nm (20-day), and ~25.24 nm and ~26.14 nm (30-day). After $ScCO_2$ treatment, the average deformations of $h_m - h_l$ for coal I6 and coal P8 are ~20.55 nm and ~28.92 nm (10-day), ~22.99 nm and ~36.20 nm (20-day), and ~22.33 nm and ~31.94 nm (30-day), and which are ~22.17 nm and ~38.93 nm (10-day), ~20.09 nm and ~41.75 nm (20-day), and ~22.56 nm and ~50.80 nm (30-day) for coal I6 and coal P8 due to $ScCO_2$-water mixture treatment. It can be observed that an obvious increase in the creep deformation ($h_m - h_l$) under constant load of 10000 μ N especially for both coal I6 and coal P8. Typically, the $ScCO_2$-water mixture environment can cause a significant increase in the creep deformation for coal I6, followed by the $ScCO_2$ environment condition. By comparing with sub-bituminous I6 and bituminous coal P8, the bituminous coal P8 exhibits relatively smaller creep deformations. In other words, the bituminous coal P8 is expected to better withhold mechanical compressions under the constant load and the coal is 'hard' enough to avoid permanent deformation responses, which implicitly in consistent with the results in Fig. 6 showing that the coal I6 is prone to occur deformation under same stress condition.

After the holding stage, the unloading stage can help us understand the deformation recoverability of two coals. The deformation recoveries ($h_m - h_f$) were calculated and plotted in Fig. 9. For coal I6 and coal P8, the average deformation recoveries ($h_m - h_f$) at initial time are ~655.75 nm and ~741.41 nm, respectively. After gaseous CO_2 treatment, the average deformation recoveries ($h_m - h_f$) for coal I6 and coal P8 are ~711.20 nm and ~809.35 nm (10-day), ~674.30 nm and ~743.82 nm (20-day), and ~690.12 nm and ~690.77 nm (30-day). After $ScCO_2$ treatment, average deformation recoveries ($h_m - h_f$) for coal I6 and coal P8 are ~692.92 nm and ~916.19 nm (10-day), ~685.87 nm and ~843.17 nm (20-day), and ~681.12 nm and ~807.03 nm (30-day), and which are ~714.10 nm and ~1012.22 nm (10-day), ~668.15 nm and ~961.87 nm (20-day), and ~639.74 nm and ~1025.97 nm (30-day) for coal I6 and coal P8 due to $ScCO_2$-water mixture treatment. In addition, it can be found that the deformation recoverability of bituminous coal P8 is worse than sub-bituminous coal I6. In other words, the harder bituminous coal is more brittle than sub-bituminous coal, which is expected to better in stiffer, but the deformations are relatively permanent upon the deformation occur.

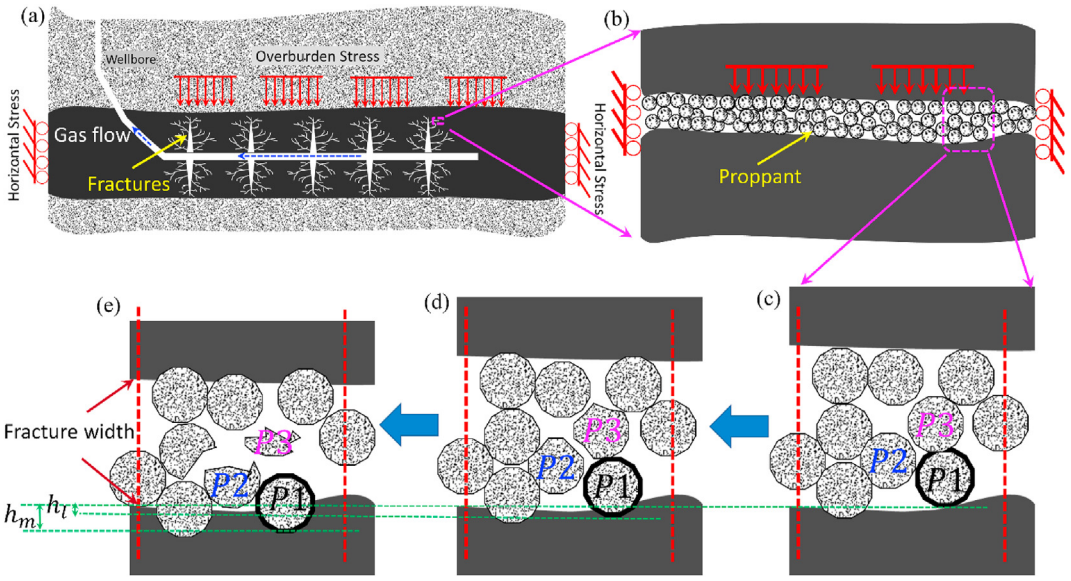

Fig. 7. Schematic of the loading deformation variations of proppants and stressed coal, and the associated proppant crushing (proppants 'P2' and 'P3'), proppant embedment (proppant 'P1'). (a) Hydraulic fracturing scheme. (b) Proppant distributions in fractured coal. (c) Early-stage status of proppant distribution. (d) proppant crushing or embedment under the dynamic stress condition. (e) Relatively stable status of proppant distribution during upon the stress condition tend to become stable.

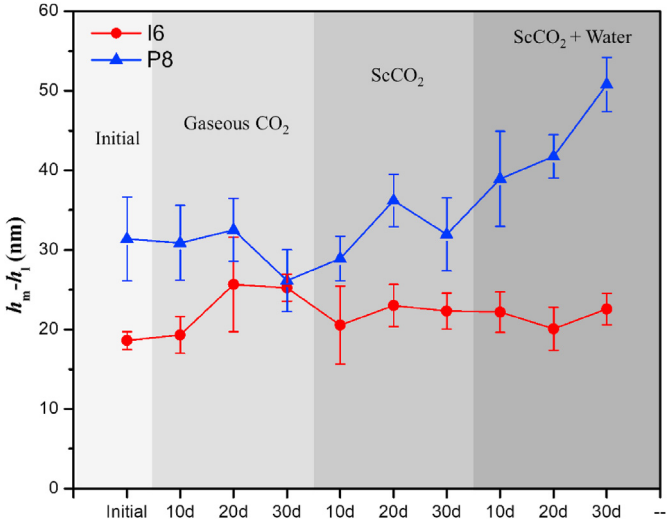

Fig. 8. Deformation increases ($h_m - h_l$) beneath the pointed indenter during holding stage.

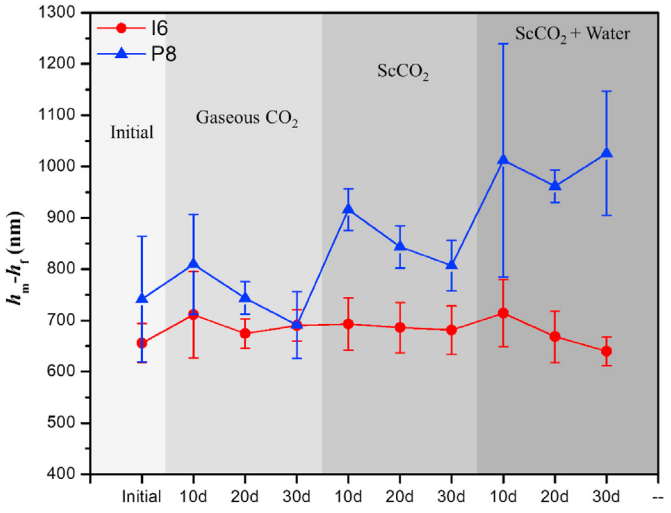

Fig. 9. Deformation recoveries ($h_m - h_f$) beneath the pointed indenter during the unloading stage.

3.5. *Irreversible plastic work in response to the mechanical deformation before and after CO_2 fluids treatments*

Based on the analysis of the energy dissipated during the nanoindentation test, the total work can be defined as:

$$U_t = \int P dh, \tag{8}$$

where U_t is the total work. During the indentation, the total work is transformed into the elastic strain energy U_e, the energy dissipated due to fracture U_f, the energy dissipated due to plastic deformation U_p and thermal energy D, giving by:

$$U_t = U_e + U_f + U_p + D, \tag{9}$$

In Eq. (9), the elastic strain energy is reversible while the other contributions are irreversible. The amount of energy dissipated during a complete loading-unloading cycle equal $U_{ir} = U_f + U_p + D$, which is equivalent to the area between the loading and unloading curve, as illustrated in Fig. 10.

The nonlinear loading and unloading curves are concave upwards and can be fit by power-law functions:

$$P_{l,h} = P_{max}\left(\frac{h}{h_l}\right)^n, \tag{10}$$

$$P_{u,h} = P_{max}\left(\frac{h - h_f}{h_m - h_f}\right)^m, \tag{11}$$

where n and m are the power indexes for the loading and unloading indentation curves.

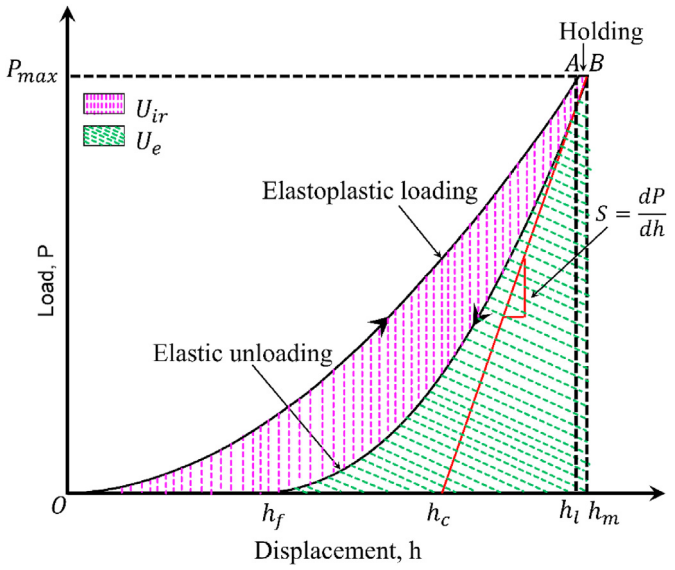

Fig. 10. Energy dissipation during the nanoindentation test.

The total energy U_t and the elastic strain energy U_e can be calculated by integrating the loading and unloading curves, respectively,

$$U_t = \int_0^{h_l} P_{l,h}dh + \int_{h_l}^{h_m} P_m dh = P_m\left(h_m - \frac{n}{1+n}h_l\right) \tag{12}$$

$$U_e = \int_{h_f}^{h_m} P_{u,h}dh = \frac{P_m\left(h_m - h_f\right)}{m+1} \tag{13}$$

The irreversible energy ratio can be easily obtained by:

$$\frac{U_{ir}}{U_t} = 1 - \frac{U_e}{U_t} = 1 - \frac{(n+1)\left(h_m - h_f\right)}{(m+1)(h_m + nh_m - nh_l)} \tag{14}$$

Eq. (14) gives the irreversible energy ratio by considering the holding stage during the nanoindentation test.

As quantified in from Eq. (8) to Eq. (14), the energy dissipations during the loading-holding-unloading nanoindentation test are illustrated in Fig. 10, among which the irreversible energy is energy used for grain loosening, crack propagation, inter-grain friction et al. Based on Eqs. (10) and (11), the loading and unloading curves were fitted to obtain the exponents 'n' and 'm' for calculating the irreversible work ratios defined in Eq. (14). The irreversible work ratios of two samples were plotted in Fig. 11. For coal I6, the initial irreversible work ratios range from ~0.17 to ~0.75 with an average of ~0.46, while the irreversible work ratios range from ~0.41 to

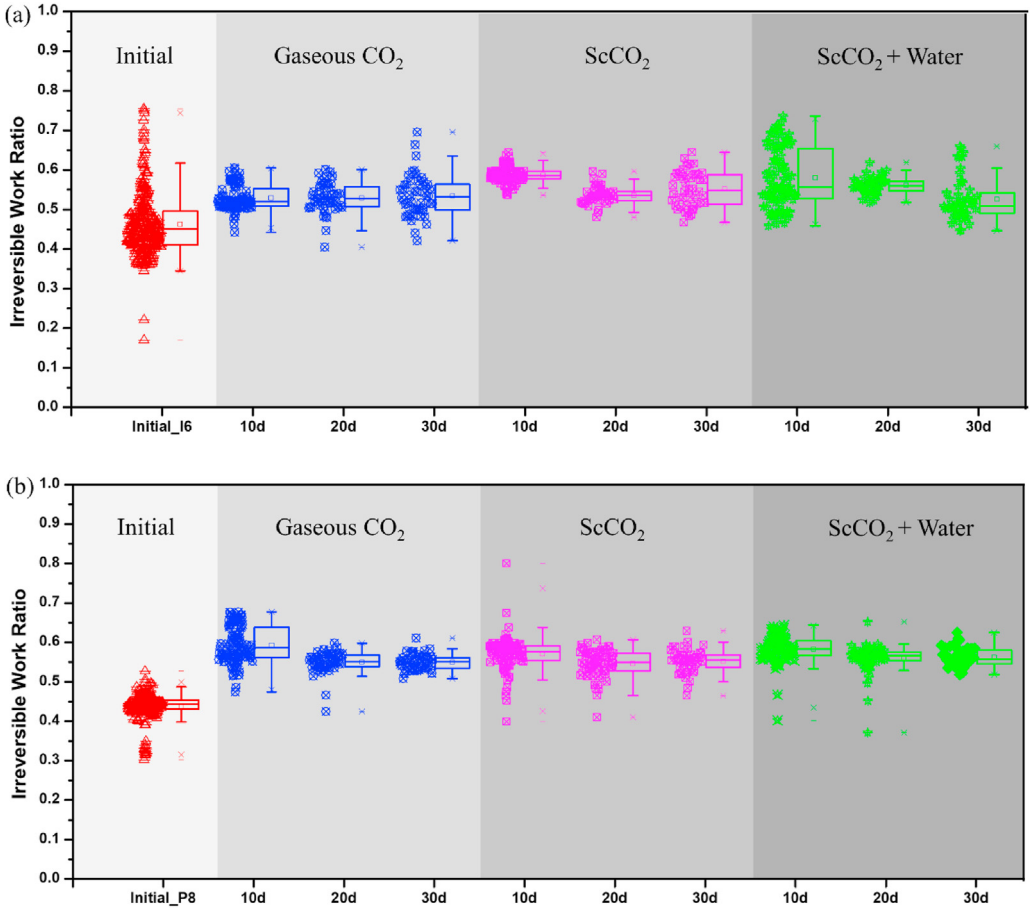

Fig. 11. Alterations on irreversible work of two coals under different treatment conditions. (a) coal I6; (b) coal P8.

~0.70 with an average of ~0.53 after gaseous CO_2 treatment, from ~0.47 to ~0.64 with an average of ~0.57 after $ScCO_2$ treatment, from ~0.45 to ~0.74 with an average of ~0.56 after '$ScCO_2$+water' treatment. For coal P8, the initial irreversible work ratios range from ~0.30 to ~0.53 with an average of ~0.44, while the irreversible work ratios range from ~0.42 to ~0.68 with an average of ~0.57 after gaseous CO_2 treatment, from ~0.40 to ~0.80 with an average of ~0.56 after $ScCO_2$ treatment, from ~0.37 to ~0.65 with an average of ~0.57 after '$ScCO_2$+water' treatment. The increase in the irreversible work ratios on coal I6 due to gaseous CO_2, $ScCO_2$, and $ScCO_2$-water mixture treatments can be up to ~1.15 times, ~1.24 times, and ~1.22 times, respectively, while for coal P8 the increases can be up to ~1.30 times, ~1.27 times, and ~1.30times. Based on the Griffith-Irwin theory [22,42,43], a pre-existing crack with certain length begins to grow when the stress intensity factor at the crack tip exceeds the fracture toughness K_C ($K_C = \sqrt{\frac{E_r U_f}{A_f}}$, where A_f is the surface area of fracture, U_f is the energy disspated due to fracture, E_r is the reduced modulus) of the solid matrix. We can see that the fracture toughness is proportional to the fracture energy and further the fracture energy is a partial of the total irreversible energy based on Eq. (9). Thus, the increase in the irrecerible work ratios potententially decrease the fracture toughness. In othe words, after gaseous CO_2, $ScCO_2$, and $ScCO_2$-water mixture treatments on coals, the fracture toughness tend to decrease and the resistance to the growth of the pre-existing crack with certain length was decreased.

4. Summary and conclusions

We conducted the combined grid-based nanoindentation tests and FESEM-EDS analyses to understand and quantify the mechanical properties variation and distribution of coals in micro- or nanoscale due to its mineral and structural variation. We also quantified the mechanical property alterations induced by gaseous CO_2, $ScCO_2$, and $ScCO_2$-water mixture treatments at different treating durations. The nanoscale deformation responses of two coals (one sub-bituminous and one bituminous) in terms of its modulus, hardness, and stage-based deformations and energy dissipations were analyzed. Based on the study, the following major conclusions can be summarized:

(1) The combined results from the FESEM-EDS and XRD confirmed the heterogeneous characteristics of two coals in microscale, and thus the nano- and micro-scale mechanical properties are expected to be composition- and microstructure-dependent. Thus, the heterogeneity of coal at nano-to-micron scale is prevailing and the geochemical and geophysical interactions of coal with fluids should consider the heterogeneous variations.
(2) Comparing with gaseous CO_2 and $ScCO_2$ treatments, the '$ScCO_2$+water' treatment can significantly deteriorate the hardness of two coals. The reductions in average Young's moduli of coal I6 induced by $ScCO_2$-water mixture treatments can be up to 2.25 times, followed by the $ScCO_2$ treatment of about 1.76 times and gaseous CO_2 treatment of around 1.32 times. For coal P8, very limited changes on the average Young's moduli of coal P8 were caused by gaseous CO_2 treatment with a reduction of ~12% and $ScCO_2$ treatment with a reduction of ~8% respectively, while very significant reduction of around ~2.15 times caused by '$ScCO_2$+water' treatment. This primarily due to the organic carbon-CO_2 interactions and water hydration effects in wetted coals, or potentially due to the dissolution and precipitation of minerals occurred in fluid environment typically under the $ScCO_2$-water treatment condition.
(3) An obvious increase in the average deformation h_l at the end of the loading stage from initial status to gaseous CO_2 condition, $ScCO_2$ condition, and then the $ScCO_2$-water mixture condition for coal I6. For coal P8, the changes of the average deformation h_l under different treatment conditions are less obvious than that of coal I6 does, which is mainly because the occurrence of mineral compositions at the landing positions of periodical indentation tests.
(4) The bituminous coal P8 is expected to better withhold mechanical compressions under the constant load and the coal is 'hard' enough to avoid permanent deformation responses.
(5) The increase in the irreversible work ratios on coal I6 due to gaseous CO_2, $ScCO_2$, and $ScCO_2$-water mixture treatments can be up to ~1.15 times, ~1.24 times, and ~1.22 times, respectively, while for coal P8 the increases can be up to ~1.30 times, ~1.27 times, and ~1.30times, respectively. The increase in the irreversible work ratios potentially decrease the fracture toughness.

Credit author statement

Ang Liu: Methodology, Investigation, Formal analysis, Writing – original draft. **Shimin Liu**: Conceptualization, Writing – review & editing.

Declaration of competing interest

The authors declare that they have no known competing financial interests or personal relationships that could have appeared to influence the work reported in this paper.

Acknowledgement

This work was financially supported by The National Institute for Occupational Safety and Health (NIOSH) under contract No. NIOSH-75D30119C05128.

Appendix A

To identify the mineral or organic carbon compositions at the landing positions of indents, FESEM-EDS and XRD are combined to match the elemental distribution layers and the potential mineral crystalline solids. As an example, the XRD fitting for coal I6 was conducted to identify the mineral crystalline compositions in coal, and thus the elemental compositions of different minerals based on their chemical expressions, as shown in Fig.A1. The EDS layered FESEM image containing a matrix of indents was shown in Fig.A2

(a), and the elemental distribution spectrum was plotted in Fig.A2 (b). Further, the overlapped elemental layers can be separated in Fig.A3. From Fig.A3, it can be very obvious to identify the occurrence of pyrite (location 'L1' in Fig. A1) by combining elemental layers of sulfur (S) and iron (Fe). Also, we can select interested areas such as locations 'L1', 'L2', 'L3', 'L4', 'L5', 'L6' to focus. The specified elemental distribution spectrums for selected areas from Fig.A2 was shown in Fig. A4. For example, location 'L1' contains chemical elements 'C', 'O', 'Fe', 'S' and the possible crystalline solid there should be pyrite-rich mineral based on Fig. A1. Location 'L2' contains chemical elements 'C', 'O', 'Al', 'Si' and the possible crystalline solid there should be kaolinite-rich mineral based on Fig. A1. Locations 'L4' and 'L5' only contains chemical elements 'C' and these areas should be organic carbon-rich areas based on Fig. A1.

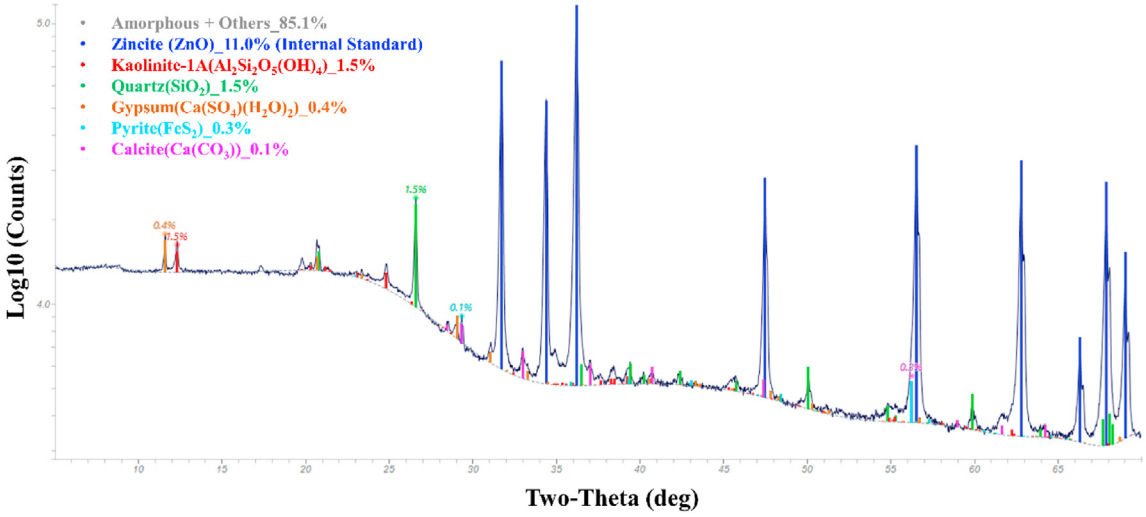

Fig. A1. Mineral composition identification using XRD fitting (I6)

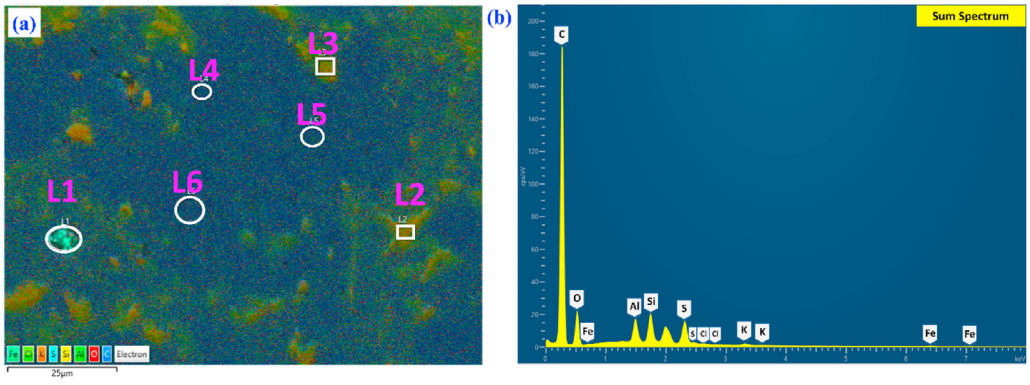

Fig. A2. EDS layered FESEM images (a) and elemental distribution spectrum (b).

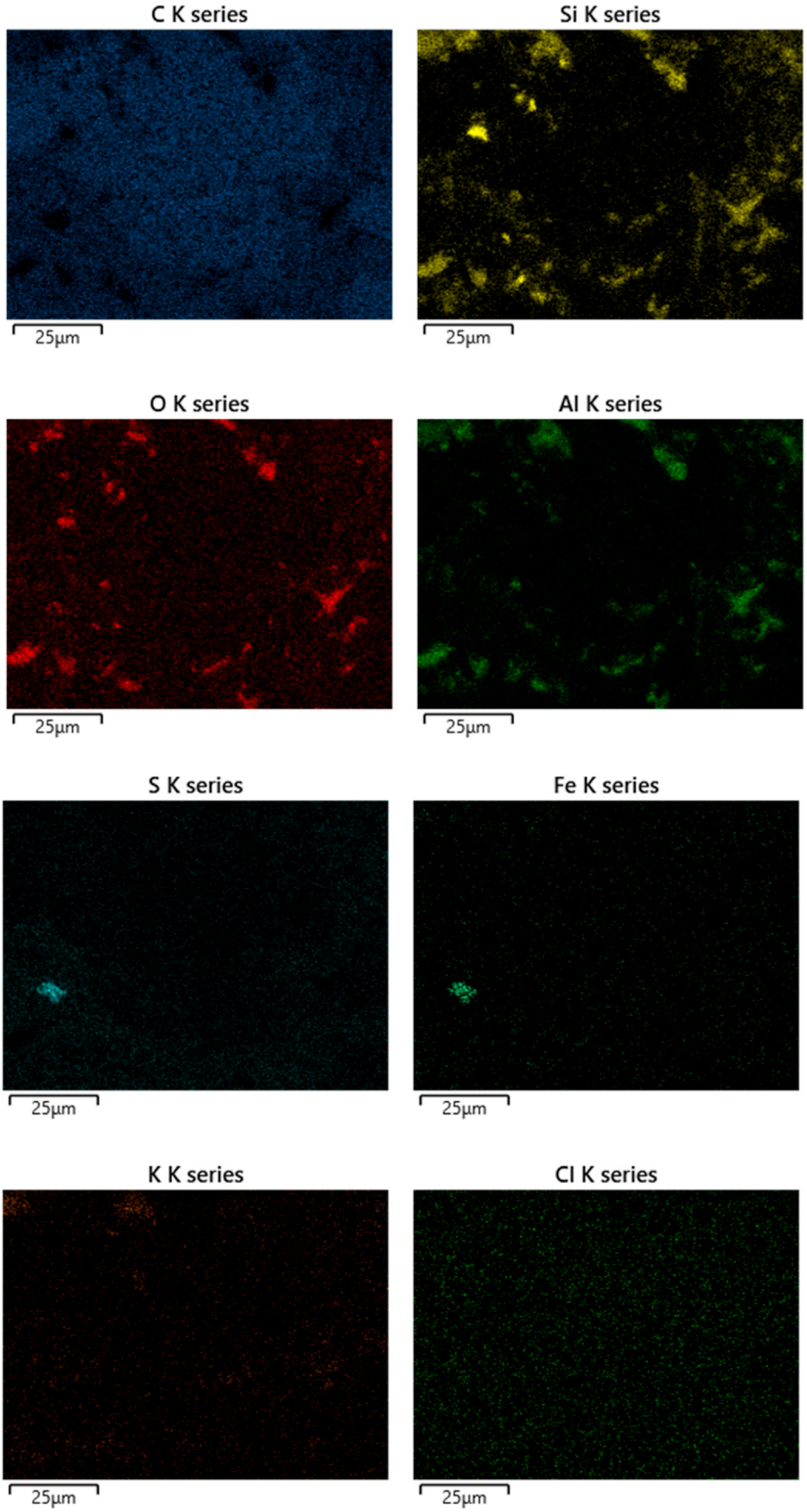

Fig. A3. Specified elemental distribution including carbon (C), oxygen (O), silicon (Si), aluminum (Al), sulfur (S), potassium (K), iron (Fe), and chlorine (Cl).

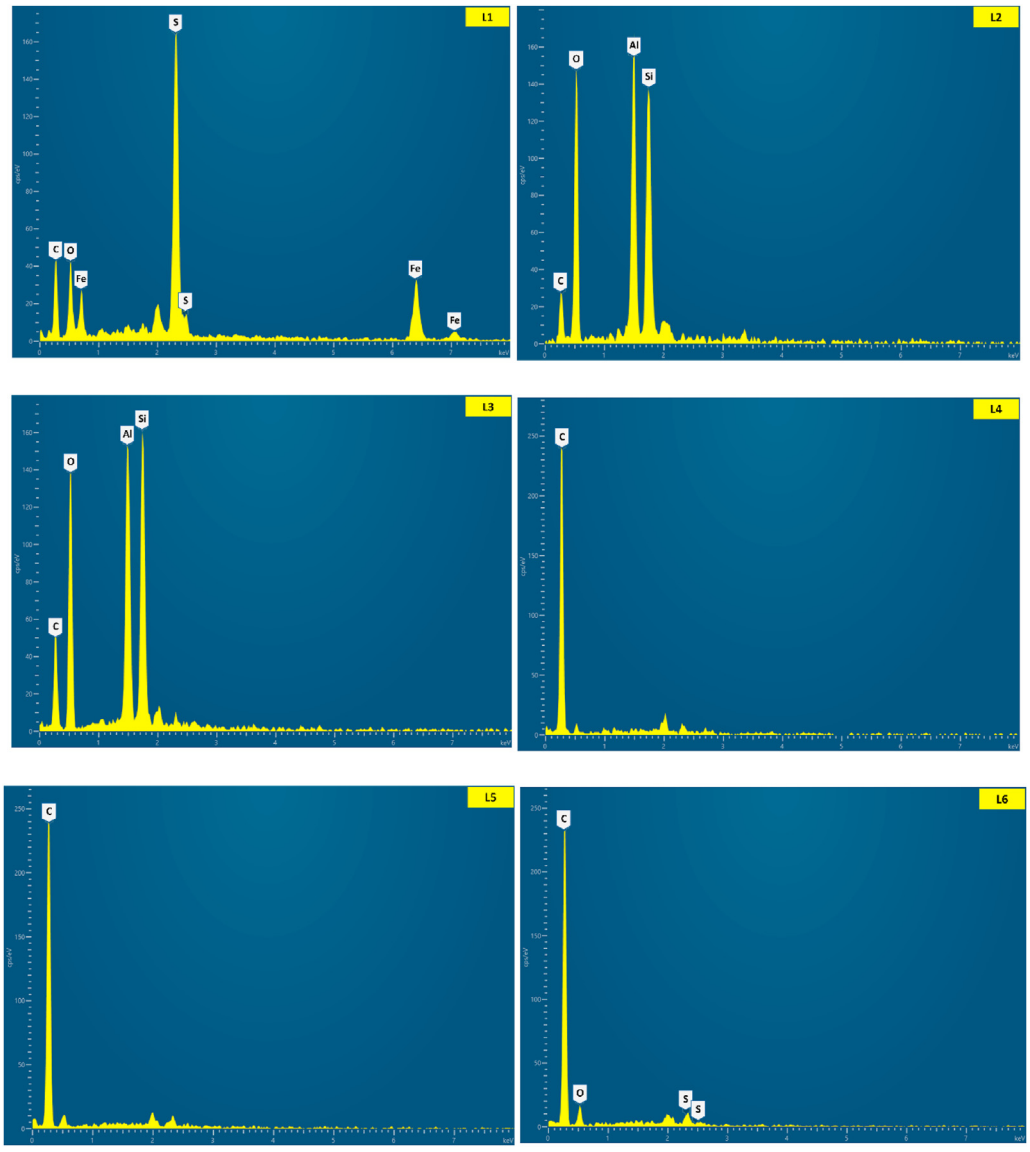

Fig. A4. Specified elemental distribution spectrums for selected areas from Fig.A2.

Appendix B

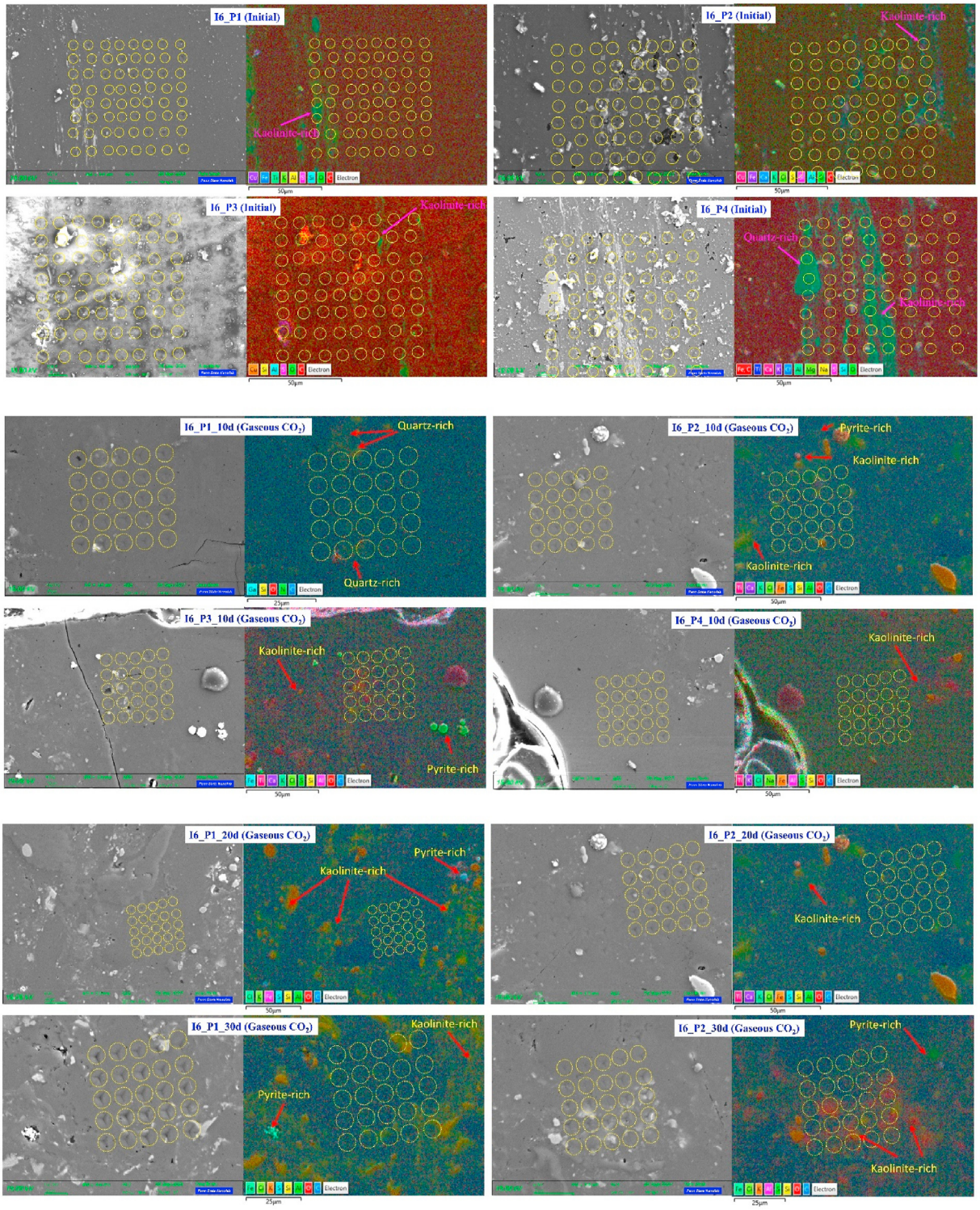

Fig. B1. EDS map overlayed FESEM image showing localized morphology characteristics and organic/mineral compositions at the landing positions of indents.

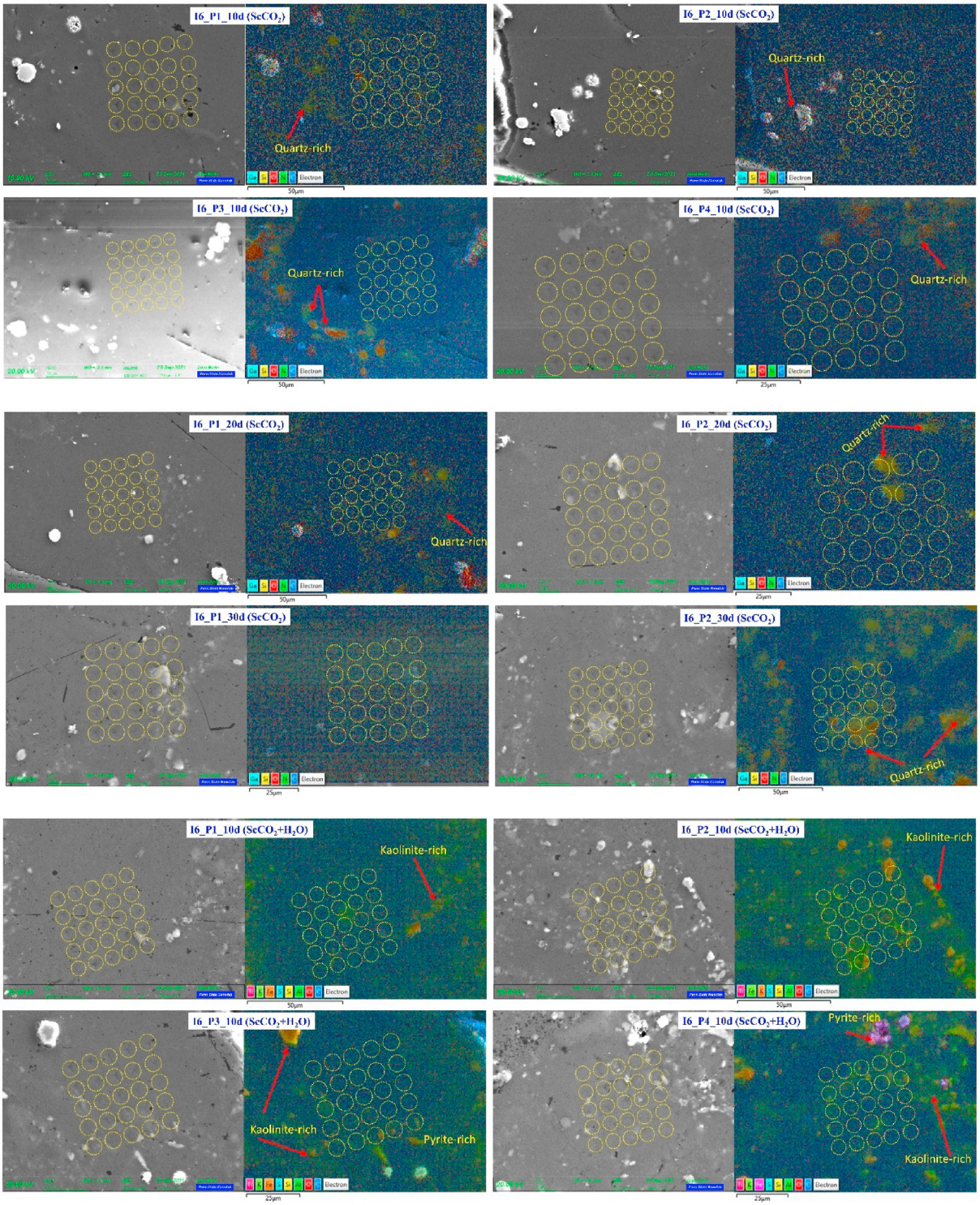

Fig. B1. (*continued*).

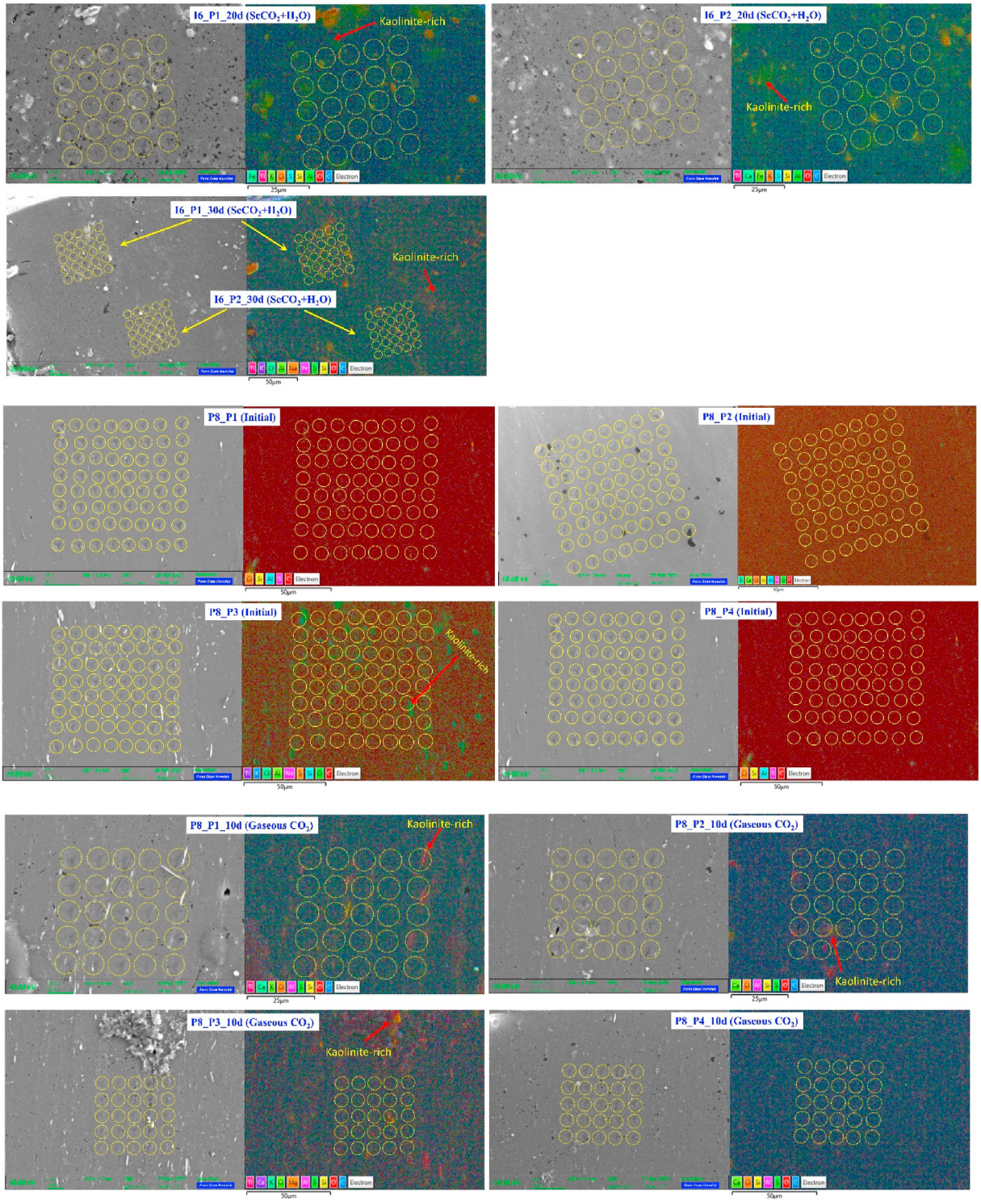

Fig. B1. (*continued*).

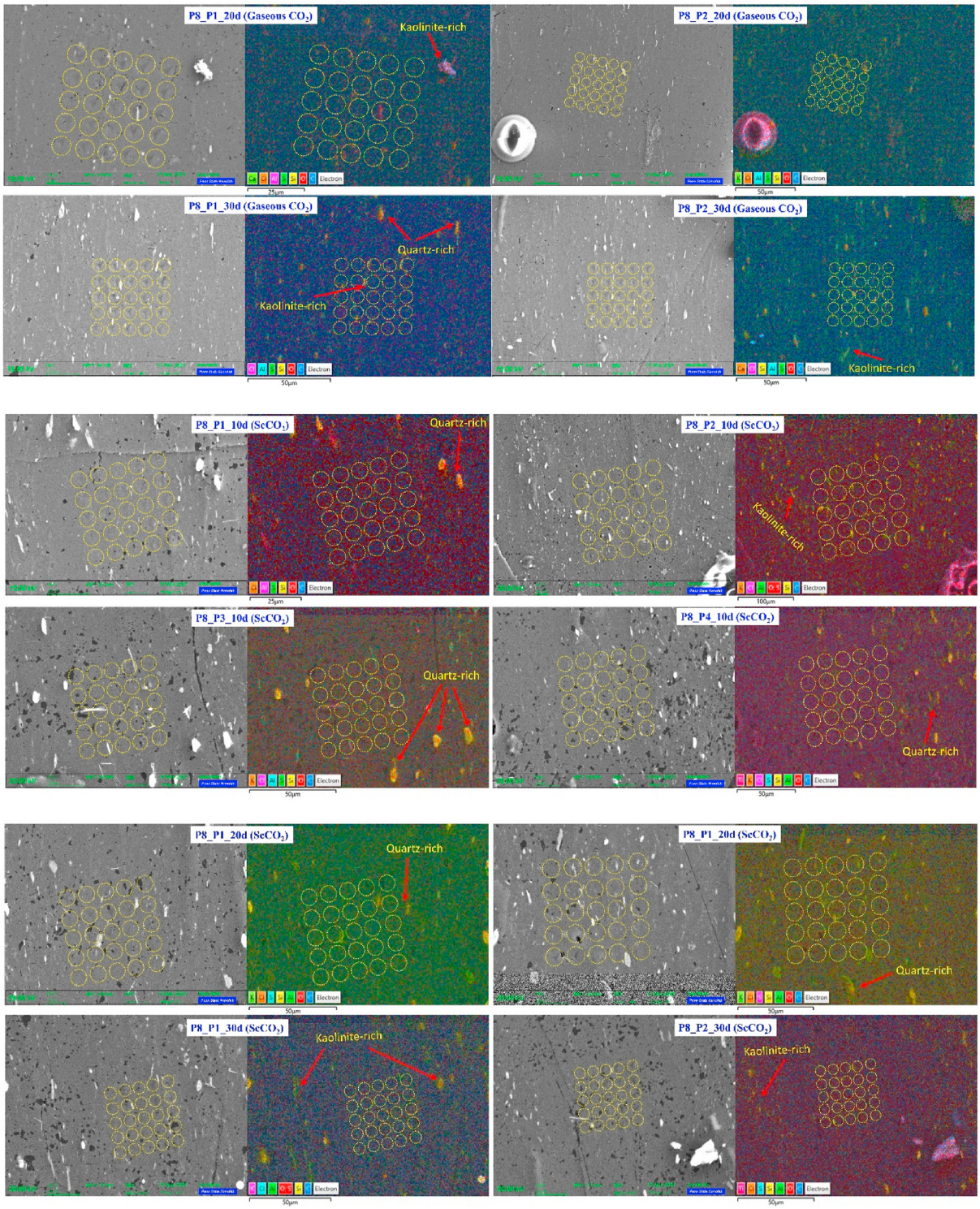

Fig. B1. (*continued*).

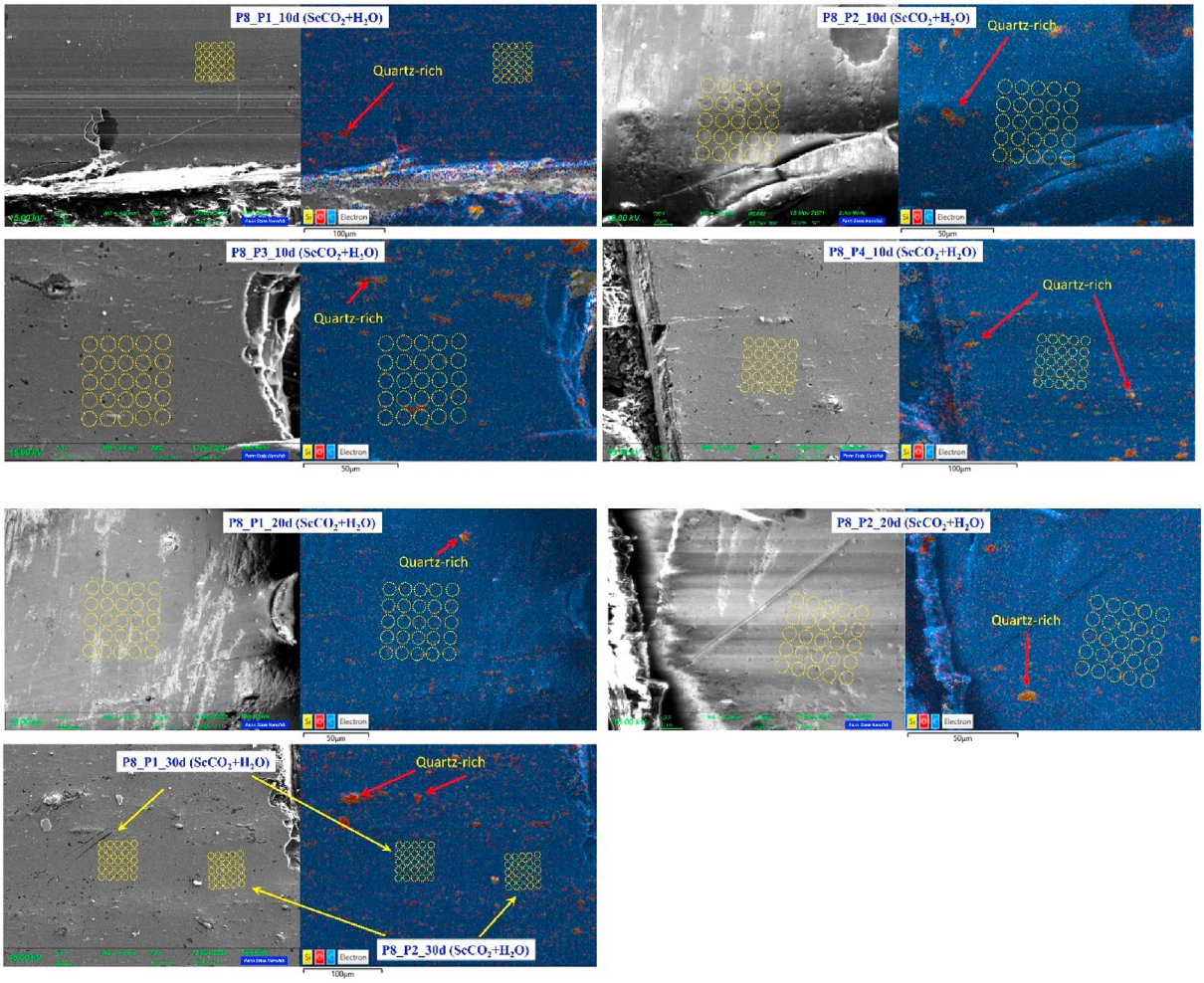

Fig. B1. (*continued*).

References

[1] Haszeldine RS. Carbon capture and storage: how green can black be? Science 2009;325:1647–52. https://doi.org/10.1126/science.1172246.

[2] Pacala S, Socolow R. Stabilization wedges: solving the climate problem for the next 50 years with current technologies. Science 2004;305:968–72. https://doi.org/10.1126/science.1100103.

[3] Chaturvedi KR, Trivedi J, Sharma T. Single-step silica nanofluid for improved carbon dioxide flow and reduced formation damage in porous media for carbon utilization. Energy 2020;197:117276. https://doi.org/10.1016/j.energy.2020.117276.

[4] Chaturvedi KR, Narukulla R, Amani M, Sharma T. Experimental investigations to evaluate surfactant role on absorption capacity of nanofluid for CO_2 utilization in sustainable crude mobilization. Energy 2021;225:120321. https://doi.org/10.1016/j.energy.2021.120321.

[5] Fujioka M, Yamaguchi S, Nako M. CO_2-ECBM field tests in the ishikari coal basin of Japan. Int J Coal Geol 2010;82:287–98. https://doi.org/10.1016/j.coal.2010.01.004.

[6] Lal R. Sequestration of atmospheric CO_2 in global carbon pools. Energy Environ Sci 2008;1:86–100. https://doi.org/10.1039/b809492f.

[7] Perera MSA, Ranjith PG, Viete DR. Effects of gaseous and super-critical carbon dioxide saturation on the mechanical properties of bituminous coal from the Southern Sydney Basin. Appl Energy 2013;110:73–81. https://doi.org/10.1016/j.apenergy.2013.03.069.

[8] Liu S, Wang Y, Hapalani S. Anisotropy characteristics of coal shrinkage/swelling and its impact on coal permeability evolution with CO_2 injection. Greenh Gases Sci Technol 2016;62:615–32. https://doi.org/10.1002/ghg.

[9] Liu A, Liu S, Wang G, Sang G. Modeling of coal matrix apparent strains for sorbing gases using a transversely isotropic approach. Rock Mech Rock Eng 2020. https://doi.org/10.1007/s00603-020-02159-3.

[10] Liu A, Liu S, Liu P, Harpalani S. The role of sorption-induced coal matrix shrinkage on permeability and stress evolutions under replicated in situ condition for CBM reservoirs. Fuel 2021;294:120530. https://doi.org/10.1016/j.fuel.2021.120530.

[11] Liu A, Liu S. Water sorption on coal: effects of oxygen containing function groups and pore structure. Int J Coal Sci Technol 2021. https://doi.org/10.1007/s40789-021-00424-6.

[12] Liu A, Liu S. A fully-coupled water-vapor flow and rock deformation/damage model for shale and coal : its application for mine stability evaluation. Int J Rock Mech Min Sci 2021;146:104880. https://doi.org/10.1016/j.ijrmms.2021.104880.

[13] Kim BH, Walton G, Larson MK, Berry S. Investigation of the anisotropic confinement-dependent brittleness of a Utah coal. Int J Coal Sci Technol 2021;8:274–90. https://doi.org/10.1007/s40789-020-00364-7.

[14] Dou L, Yang K, Chi X. Fracture behavior and acoustic emission characteristics of sandstone samples with inclined precracks. Int J Coal Sci Technol 2021;8:77–87. https://doi.org/10.1007/s40789-020-00344-x.

[15] Zuo J, Wang J, Jiang Y. Macro/meso failure behavior of surrounding rock in deep roadway and its control technology. Int J Coal Sci Technol 2019;6:301–19. https://doi.org/10.1007/s40789-019-0259-0.

[16] Masoudian MS, Airey DW, El-Zein A. Experimental investigations on the effect of CO_2 on mechanics of coal. Int J Coal Geol 2014;128–129:12–23. https://doi.org/10.1016/j.coal.2014.04.001.

[17] Hol S, Spiers CJ, Peach CJ. Microfracturing of coal due to interaction with CO_2 under unconfined conditions. Fuel 2012;97:569–84. https://doi.org/10.1016/j.fuel.2012.02.030.

[18] Sampath KHSM, Perera MSA, Ranjith PG, Matthai SK, Tao X, Wu B. Application of neural networks and fuzzy systems for the intelligent prediction of CO2-induced strength alteration of coal. Measurement 2019;135:47–60. https://doi.org/10.1016/j.measurement.2018.11.031.

[19] Bhushan B, Li X. Nanomechanical characterisation of solid surfaces and thin films. Int Mater Rev 2003;48:125–64. https://doi.org/10.1179/

095066003225010227.
[20] Oliver WC, Pharr GM. An improved technique for determining hardness and elastic modulus using load and displacement sensing indentation experiments. J Mater 1992;7:1564–83.
[21] Kumar V, Sondergeld CH, Rai CS. Nano to macro mechanical characterization of shale. SPE Annu Tech Conf Exhib 2012;4:3421–43. https://doi.org/10.2118/159804-ms.
[22] Manjunath GL, Jha B. Nanoscale fracture mechanics of Gondwana coal. Int J Coal Geol 2019;204:102–12. https://doi.org/10.1016/j.coal.2019.02.007.
[23] Berthonneau J, Hoover CG, Grauby O, Baronnet A, Pellenq RJM, Ulm FJ. Crystal-chemistry control of the mechanical properties of 2:1 clay minerals. Appl Clay Sci 2017;143:387–98. https://doi.org/10.1016/j.clay.2017.04.010.
[24] Viktorov SD, Golovin YI, Kochanov AN, Tyurin AI, Shuklinov AV, Shuvarin IA, et al. Micro- and nano-indentation approach to strength and deformation characteristics of minerals. J Min Sci 2015;50:652–9. https://doi.org/10.1134/S1062739114040048.
[25] Thom CA, Carpick RW, Goldsby DL. Constraints on the physical mechanism of frictional aging from nanoindentation. Geophys Res Lett 2018;45(13):306–13. https://doi.org/10.1029/2018GL080561.
[26] Shukla P, Kumar V, Curtis M, Sondergeld CH, Rai CS. Nanoindentation studies on shales. 47th US Rock Mech/Geomech Symp 2013;2:1194–203.
[27] Zhang Y, Lebedev M, Al-Yaseri A, Yu H, Xu X, Iglauer S. Characterization of nanoscale rockmechanical properties and microstructures of a Chinese sub-bituminous coal. J Nat Gas Sci Eng 2018;52:106–16. https://doi.org/10.1016/j.jngse.2018.01.037.
[28] Zhang Y, Lebedev M, Smith G, Jing Y, Busch A, Iglauer S. Nano-mechanical properties and pore-scale characterization of different rank coals. Nat Resour Res 2020;29:1787–800. https://doi.org/10.1007/s11053-019-09572-8.
[29] Ma Z, Pathegama Gamage R, Zhang C. Application of nanoindentation technology in rocks: a review. Geomech Geophys Geo Energy Geo Resour 2020;6:1–27. https://doi.org/10.1007/s40948-020-00178-6.
[30] Luo S, Wu Y, Li Y, Wang D, Kim D, Song J, et al. Nanoindentation-enhanced screening of hydraulic fracturing fluid additives. Int J Coal Geol 2021;240:103744. https://doi.org/10.1016/j.coal.2021.103744.
[31] Oliver DJ, Lawn BR, Cook RF, Reitsma MG, Bradby JE, Williams JS, et al. Giant pop-ins in nanoindented silicon and germanium caused by lateral cracking. J Mater Res 2008;23:297–301. https://doi.org/10.1557/jmr.2008.0070.
[32] Oliver WC, Pharr GM. Measurement of hardness and elastic modulus by instrumented indentation: advances in understanding and refinements to methodology. J Mater Res 2004;19:3–20. https://doi.org/10.1557/jmr.2004.19.1.3.
[33] Sneddon IN. The relation between load and penetration in the axisymmetric boussinesq problem for a punch of arbitrary profile. Int J Eng Sci 1965;3:47–57. https://doi.org/10.1016/0020-7225(65)90019-4.
[34] Yu H, Zhang Y, Lebedev M, Han T, Verrall M, Wang Z, et al. Nanoscale geomechanical properties of Western Australian coal. J Petrol Sci Eng 2018;162:736–46. https://doi.org/10.1016/j.petrol.2017.11.001.
[35] Borodich FM, Bull SJ, Epshtein SA. Nanoindentation in studying mechanical properties of heterogeneous materials. J Min Sci 2015;51:470–6. https://doi.org/10.1134/S1062739115030072.
[36] Epshtein SA, Borodich FM, Bull SJ. Evaluation of elastic modulus and hardness of highly inhomogeneous materials by nanoindentation. Appl Phys Mater Sci Process 2015;119:325–35. https://doi.org/10.1007/s00339-014-8971-5.
[37] Shi X, Jiang S, Wang Z, Bai B, Xiao D, Tang M. Application of nanoindentation technology for characterizing the mechanical properties of shale before and after supercritical CO_2 fluid treatment. J CO2 Util 2020;37:158–72. https://doi.org/10.1016/j.jcou.2019.11.022.
[38] Zhang Y, Lebedev M, Al-Yaseri A, Yu H, Xu X, Sarmadivaleh M, et al. Nanoscale rock mechanical property changes in heterogeneous coal after water adsorption. Fuel 2018;218:23–32. https://doi.org/10.1016/j.fuel.2018.01.006.
[39] Zhang R, Liu S, Zheng S. Characterization of nano-to-micron sized respirable coal dust: particle surface alteration and the health impact. J Hazard Mater 2021;413:125447. https://doi.org/10.1016/j.jhazmat.2021.125447.
[40] Ozotta O, Ostadhassan M, Liu K, Liu B, Kolawole O, Hadavimoghaddam F. Reassessment of CO2 sequestration in tight reservoirs and associated formations. J Petrol Sci Eng 2021;206:109071. https://doi.org/10.1016/j.petrol.2021.109071.
[41] Prakash R, Kana Nguene PC, Benoit D, Henkel K, Abedi S. Assessment of local phase to mechanical response link: application to the chemo-mechanical identification of rock phases subjected to reactive environments. J Nat Gas Sci Eng 2021:89. https://doi.org/10.1016/j.jngse.2021.103857.
[42] Irwin GR. Fracture. In: Flugge S, editor. Handbuch der Physik, vol. 6. Berlin: Springer- Verlag; 1958. p. 551–90.
[43] Griffith AA. The phenomena of rupture and flow in solids. Philos Trans R Soc Lond Ser 1921;221:163–98.